Autophagy Regulation of Metabolism Is Required for CD8+ T Cell Anti-tumor Immunity

Lindsay DeVorkin, Nils Pavey, Gillian Carleton, Alexandra Comber, Cally Ho, Junghyun Lim, Erin McNamara, Haochu Huang, Paul Kim, Lauren G. Zacharias, Noboru Mizushima, Tatsuya Saitoh, Shizuo Akira, Wayne Beckham, Alireza Lorzadeh, Michelle Moksa, Qi Cao, Aditya Murthy, Martin Hirst, Ralph J. DeBerardinis, Julian J. Lum

April 2019

This article was originally published at:

https://doi.org/10.1016/j.celrep.2019.03.037

Citation for this paper:

DeVorkin, L., Pavey, N., Carleton, G., Comber, A., Ho, C., Lim, J. & Lum, J.J. (2019). Autophagy Regulation of Metabolism Is Required for CD8+ T Cell Anti-tumor Immunity. *Cell Reports, 27*(2), 502-513.e5.
https://doi.org/10.1016/j.celrep.2019.03.037

Cell Reports

Article

Autophagy Regulation of Metabolism Is Required for CD8$^+$ T Cell Anti-tumor Immunity

Graphical Abstract

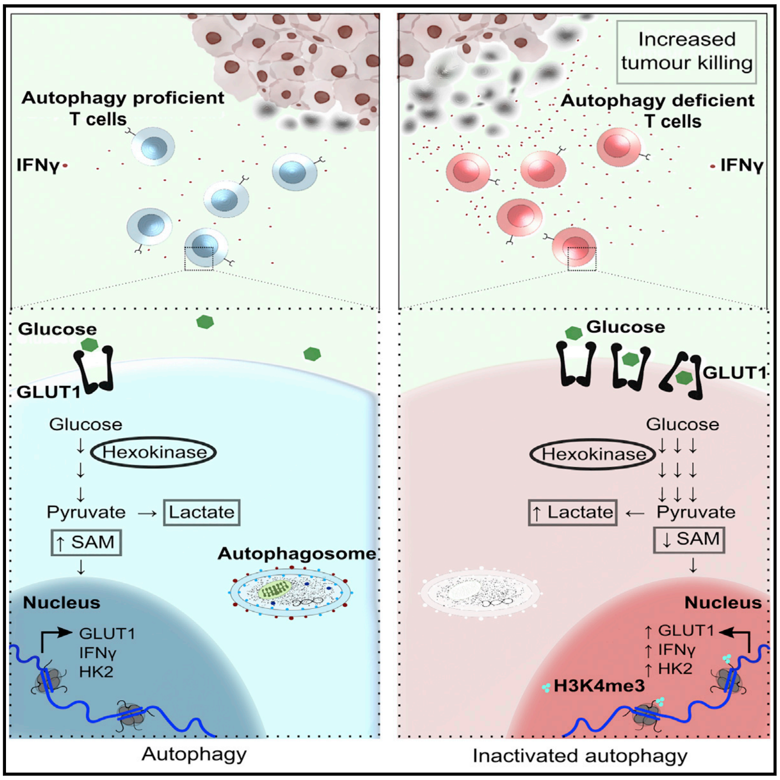

Highlights

- Inactivation of T cell autophagy results in enhanced tumor rejection
- T cells deficient in autophagy show increased glucose uptake and lactate production
- Reduction in SAM transcriptionally reprograms immune cells toward effector memory

Authors

Lindsay DeVorkin, Nils Pavey, Gillian Carleton, ..., Martin Hirst, Ralph J. DeBerardinis, Julian J. Lum

Correspondence

jjlum@bccancer.bc.ca

In Brief

DeVorkin et al. show that loss of autophagy enhances CD8$^+$ T-cell-mediated rejection of tumors. Mechanistically, suppression of autophagy shifts T cells to a glycolytic phenotype and causes a reduction in S-adenosylmethionine. As a consequence, autophagy-deficient T cells transcriptionally reprogram immune response genes to an effector memory state.

DeVorkin et al., 2019, Cell Reports *27*, 502–513
April 9, 2019 Crown Copyright © 2019
https://doi.org/10.1016/j.celrep.2019.03.037

OPEN
ACCESS
CellPress

Cell Reports
Article

Autophagy Regulation of Metabolism Is Required for CD8$^+$ T Cell Anti-tumor Immunity

Lindsay DeVorkin,[1] Nils Pavey,[1] Gillian Carleton,[1,2,14] Alexandra Comber,[1,14] Cally Ho,[1,2] Junghyun Lim,[3] Erin McNamara,[4] Haochu Huang,[4] Paul Kim,[1,2] Lauren G. Zacharias,[5] Noboru Mizushima,[6] Tatsuya Saitoh,[7] Shizuo Akira,[8] Wayne Beckham,[9,10] Alireza Lorzadeh,[11] Michelle Moksa,[11] Qi Cao,[11] Aditya Murthy,[3] Martin Hirst,[11,12] Ralph J. DeBerardinis,[13] and Julian J. Lum[1,2,15,*]

[1]Trev and Joyce Deeley Research Centre, BC Cancer, Victoria, BC, Canada
[2]Department of Biochemistry and Microbiology, University of Victoria, Victoria, BC, Canada
[3]Department of Cancer Immunology, Genentech, Inc., South San Francisco, CA, USA
[4]Department of In Vivo Pharmacology, Genentech, Inc., South San Francisco, CA, USA
[5]Children's Medical Center Research Institute, University of Texas Southwestern Medical Center, Dallas, TX, USA
[6]Department of Biochemistry and Molecular Biology, Graduate School and Faculty of Medicine, The University of Tokyo, Tokyo, Japan
[7]Division of Inflammation Biology, Institute for Enzyme Research, Tokushima University, Tokushima, Japan
[8]Department of Host Defense, World Premier International Immunology Frontier Research Center, Osaka University, Suita, Osaka, Japan
[9]BC Cancer-Vancouver Island Centre, Medical Physics, Victoria, BC, Canada
[10]Department of Physics and Astronomy, University of Victoria, Victoria, BC, Canada
[11]Department of Microbiology and Immunology and Michael Smith Laboratories, University of British Columbia, Vancouver, BC, Canada
[12]Canada's Michael Smith Genome Science Center, BC Cancer, Vancouver, BC, Canada
[13]Children's Medical Center Research Institute, Department of Pediatrics and McDermott Center for Human Growth and Development, University of Texas Southwestern Medical Center, Dallas, TX, USA
[14]These authors contributed equally
[15]Lead Contact
*Correspondence: jjlum@bccancer.bc.ca

https://doi.org/10.1016/j.celrep.2019.03.037

SUMMARY

Autophagy is a cell survival process essential for the regulation of immune responses to infections. However, the role of T cell autophagy in anti-tumor immunity is less clear. Here, we demonstrate a cell-autonomous role for autophagy in the regulation of CD8$^+$ T-cell-mediated control of tumors. Mice deficient for the essential autophagy genes *Atg5*, *Atg14*, or *Atg16L1* display a dramatic impairment in the growth of syngeneic tumors. Moreover, T cells lacking *Atg5* have a profound shift to an effector memory phenotype and produce greater amounts of interferon-γ (IFN-γ) and tumor necrosis factor α (TNF-α). Mechanistically, *Atg5*$^{-/-}$ CD8$^+$ T cells exhibit enhanced glucose metabolism that results in alterations in histone methylation, increases in H3K4me3 density, and transcriptional upregulation of both metabolic and effector target genes. Nonetheless, glucose restriction is sufficient to suppress Atg5-dependent increases in effector function. Thus, autophagy-dependent changes in CD8$^+$ T cell metabolism directly regulate anti-tumor immunity.

INTRODUCTION

The presence and function of effector CD8$^+$ T cells is indispensable to controlling viral infections and rejecting tumors (Shankaran et al., 2001; Wherry and Ahmed, 2004). Recent work in preclinical models as well as human clinical studies employing immunotherapy strategies has demonstrated a critical role for CD8$^+$ T cells in mediating tumor rejection. The precise pathways regulating the functions of CD8$^+$ T cells and other T cell subsets in anti-tumor responses remain unclear. In addition to serving as licensing cues, environmental signals, including cytokines, coordinate metabolic programs that fuel biosynthetic and bioenergetic requirements to promote and maintain proper states of differentiation and function (Buck et al., 2015). Beyond general changes in glycolysis or oxidative phosphorylation (OXPHOS), additional metabolic pathways are necessary for T cell activation and differentiation. For instance, citrate and the expression of citrate synthase are essential for fatty acid biosynthesis during the initiation of T cell growth (MacPherson et al., 2017). Thus, the coordination of metabolic activities is essential to allow T cells to functionally respond to certain inflammatory conditions, including pathogen infection and immunosurveillance.

Macroautophagy (autophagy) is an evolutionarily conserved metabolic program that catabolically degrades cytoplasmic components, via autophagosomes, in lysosomes for recycling. Degradation of long-lived proteins, damaged organelles, protein aggregates, and bulk cytoplasm occurs under physiological conditions and is essential to sustain cellular homeostasis. In response to stress such as nutrient deprivation or hypoxia, autophagy is upregulated and functions to promote cell survival (Lum et al., 2005). In cancer cells, autophagy can have a dual role in both tumor cell survival and death. Autophagy is also critical in shaping adaptive T cell immunity and T cell homeostasis (Townsend et al., 2012). In naive T cells, autophagy is induced following T cell receptor (TCR) and cytokine stimulation

(Hubbard et al., 2010; Li et al., 2006; Pua et al., 2009). Deletion of *Atg5*, *Atg7*, or *Atg3* impairs peripheral T cell homeostasis and T cell survival and function (Jia et al., 2011; Pua et al., 2009; Stephenson et al., 2009). Moreover, CD8$^+$ T cells lacking *Atg5* or *Atg7* acquire an effector phenotype but are unable to survive or form functional memory T cells (Jia et al., 2011; Pua et al., 2009; Puleston et al., 2014; Schlie et al., 2015; Stephenson et al., 2009; Xu et al., 2014). These studies indicate a highly dynamic role for autophagy in T-cell-mediated adaptive immune responses.

Despite the growing appreciation for the involvement of autophagy in T cell immune responses, its contribution to tumor immunity remains unclear. In one report, intestinal epithelial cell deletion of *Atg7* in a colorectal tumor model impaired tumor growth (Lévy et al., 2015). Similar findings were also observed in a polyomavirus middle T-antigen (PyMT)-driven breast cancer model where mammary cell deletion of focal adhesion kinase family interacting protein of 200 kDa (*FIP200*) resulted in loss of tumor growth (Wei et al., 2011). The ablation of *FIP200* in this study was associated with an increase in endogenous anti-tumor immune responses. Another report found that deletion of *Atg5* in a KRas^{G12D} lung cancer model enhanced tumor initiation and this was associated with increased tumor infiltration of FOXP3$^+$ T regulatory cells (Tregs). However, despite the increased rate of tumor initiation, deletion of *Atg5* impaired tumor progression and enhanced survival of tumor-bearing mice (Rao et al., 2014). Recent studies have also indicated that loss of autophagy in host tissues can impact tumor immunity. Mice deficient for gamma-aminobutyric acid receptor-associated protein (*GABARAP*) displayed a reduction in tumor growth. This was associated with increased secretion of interleukin-2 (IL-2), interferon-γ (IFN-γ), IL-1β, and IL-6 following *in vitro* stimulation of *GABARAP*$^{-/-}$ lymphocytes and macrophages (Salah et al., 2016). Moreover, deletion of *Atg7* in Tregs resulted in reduced MC38 colon carcinoma growth and enhanced tumor infiltration of CD8$^+$ T cells, suggesting that regulation of Tregs by autophagy contributes to suppressing anti-tumor immune responses (Wei et al., 2016).

Here, we demonstrate that inactivation of the essential autophagy genes *Atg5, Atg14*, or *Atg16L1* results in rejection of syngeneic mammary, prostate, and colorectal tumors. Despite a significant reduction in the total number of CD8$^+$ tumor-infiltrating lymphocytes (TIL), loss of *Atg5* causes a profound shift toward IFN-γ- and tumor necrosis factor α (TNF-α)-producing effector memory cells. Consistent with this, adoptive transfer with *Atg5*$^{-/-}$ T cells promotes tumor control. Metabolically, autophagy in CD8$^+$ T cells restrains glucose metabolism. In addition, the inactivation of autophagy is associated with a decrease in the methyl donor S-adensylmethionine (SAM). As a result, a global loss of H3K27me3 and concomitant gains in H3K4me3 was observed. The changes in histone methylation were associated with increased transcriptional activation of both metabolic and effector target genes. However, restricting glucose in *Atg5*$^{-/-}$ T cells was sufficient to suppress autophagy-dependent increases in effector function. Thus, these findings identify autophagy as a cell-autonomous negative regulator of CD8$^+$ T cell metabolism and anti-tumor immunity with implications for T cell-based immunotherapy.

RESULTS

Loss of Canonical Autophagy Promotes Tumor Rejection

To investigate the role of autophagy in tumor initiation and growth, an inducible *Atg5* knockout mouse was generated by crossing *Atg5*$^{fl/fl}$ mice to *Cre-ER*^{T2} mice, allowing temporal control of Cre-mediated *Atg5* deletion in all host tissues (Hara et al., 2006; Schlie et al., 2015). Following administration of tamoxifen, Atg5 control and knockout mice, abbreviated *Atg5*$^{+/-}$ and *Atg5*$^{-/-}$ respectively, were implanted with autophagy competent e0771 breast cancer cells into the left mammary fat pad (Figures S1A and S1B). Inactivation of autophagy was confirmed in splenocytes from *Atg5*$^{+/-}$ and *Atg5*$^{-/-}$ mice showing diminished expression of conjugated Atg12-Atg5 and loss of basal LC3-II processing (Schlie et al., 2015; Figure S1C). In both *Atg5*$^{+/-}$ and *Atg5*$^{-/-}$ mice, tumors were macroscopically detectable 2–5 days after implantation. Despite similar initiation rates, a significant reduction in tumor growth was observed in *Atg5*$^{-/-}$ mice compared to *Atg5*$^{+/-}$ mice (Figure 1A). The loss in tumor growth in the absence of *Atg5* was also observed in mice that were challenged with autophagy-competent Tramp-C2 prostate tumor cells (Figures 1B, S1D, and S1E). Histological assessment of resected e0771 tumors from *Atg5*$^{-/-}$ mice revealed a significant increase in cleaved caspase-3 compared to tumors from *Atg5*$^{+/-}$ mice (Figure 1C). In contrast, the amount of Ki-67 staining in the tumor was similar in both *Atg5*$^{+/-}$ and *Atg5*$^{-/-}$ mice (Figure 1C). The effect of *Atg5* deletion on tumor growth was also observed when *Atg5* was deleted after tumors reached 100 mm^2 (Figure 1D). No gross morphological abnormalities in the mammary fat pad were observed in *Atg5*$^{-/-}$ mice (Figure S1F) ruling out defects related to the site of implantation as an explanation for the reduction in tumor growth. Consistent with the observations above, accelerated clearance of both e0771 and MC38 tumors was observed in mice with inducible *Atg16L1* deletion in all host tissues (Figures 1E, S1G, and S1H).

We next tested the possibility that autophagy could functionally impair endogenous anti-tumor immune responses. Two separate bone marrow chimeric (BMC) mice were generated by transferring either *Atg5*$^{+/-}$ (*Atg5*$^{+/-}$ → wild-type [WT]) or *Atg5*$^{-/-}$ (*Atg5*$^{-/-}$ → WT) bone marrow into WT mice (Figure S1I). Similar to the observations above, *Atg5*$^{-/-}$ → WT BMC mice displayed a significant reduction in e0771 tumor growth compared to control *Atg5*$^{+/-}$ → WT BMC (Figure 1F). In contrast, the ability to control tumor growth was lost when *Atg5*$^{+/-}$ or *Atg5*$^{-/-}$ mice received WT bone marrow (Figures 1G and S1I). To confirm these findings, tumor growth was examined using mice with conditional *Atg14* deletion (Figures S1J–S1L). Cells with conditional *Atg14* knockout from different lineages (e.g., myeloid, mouse embryonic fibroblasts) have been reported by several groups and were found to be defective in canonical autophagy (Itakura et al., 2008; Kaizuka and Mizushima, 2015; Matsunaga et al., 2009; Nishimura et al., 2013). Moreover, LysM-Cre-*Atg14*$^{-/-}$ mice have been previously used to demonstrate an essential role for autophagy in protection against influenza and resistance to herpes virus reactivation as well as the role of autophagy in the regulation of lung inflammation (Lu et al., 2016; Park et al., 2016). Similar to the *Atg5*$^{-/-}$ BMC results

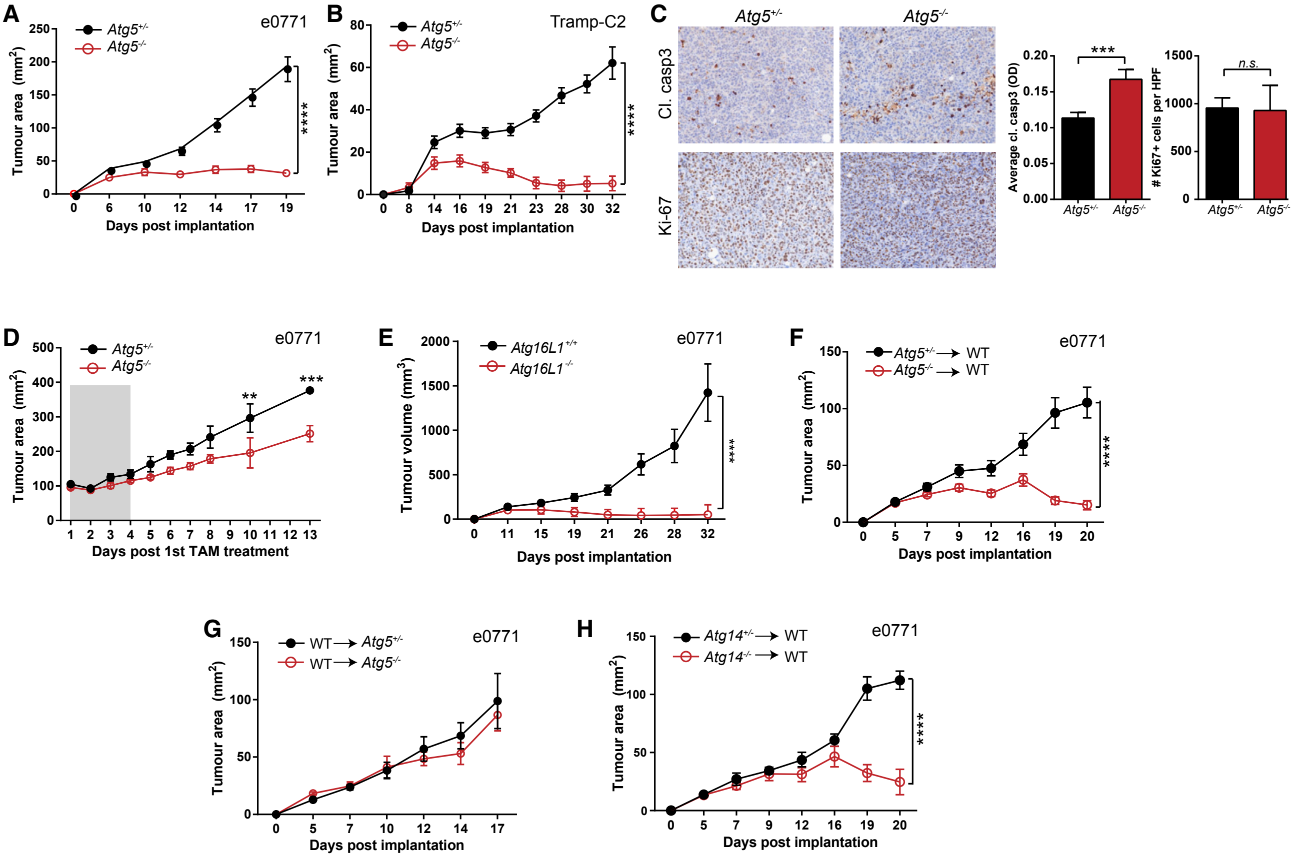

Figure 1. Autophagy Is Required for Growth of Syngeneic Breast and Prostate Tumors

(A) *Atg5*$^{+/-}$ (n = 13) and *Atg5*$^{-/-}$ (n = 11) mice were implanted with e0771 cells in the mammary fat pad, and tumor growth was monitored.

(B) Tramp-C2 cells were implanted into the flanks of *Atg5*$^{+/-}$ (n = 6) and *Atg5*$^{-/-}$ (n = 7) mice, and tumor growth was monitored.

(C) 19 days post-implantation, e0771 tumors were excised from *Atg5*$^{+/-}$ and *Atg5*$^{-/-}$ mice and stained for cleaved caspase-3 and Ki-67. Graphs show quantification of cleaved caspase-3, represented as optical density (OD), and the number of Ki-67+ cells per high-power field (HPF; n = 5 mice/group).

(D) e0771 cells were implanted into the mammary fat pad of tamoxifen-naive *Atg5*$^{+/-}$ (n = 4) and *Atg5*$^{-/-}$ (n = 5) mice. When tumors reached ~100 mm^2, tamoxifen treatment was initiated (gray box), and tumor growth was measured.

(E) *Atg16L1*$^{+/+}$ and *Atg16L1*$^{-/-}$ mice were implanted with e0771 cells in the mammary fat pad, and tumor growth was monitored (n = 10 mice per group).

(F) Lethally irradiated WT mice received BM from *Atg5*$^{+/-}$ (*Atg5*$^{+/-}$ → WT; n = 9) or *Atg5*$^{-/-}$ (*Atg5*$^{-/-}$ → WT; n = 10) mice and were implanted with e0771 cells in the mammary fat pad, and tumor growth was monitored.

(G) Lethally irradiated *Atg5*$^{+/-}$ (n = 4) or *Atg5*$^{-/-}$ (n = 4) mice received BM from WT mice and were implanted with e0771 cells in the mammary fat pad, and tumor growth was monitored.

(H) Lethally irradiated WT mice received BM from *Atg14*$^{+/-}$ (*Atg14*$^{+/-}$ → WT; n = 5) or *Atg14*$^{-/-}$ (*Atg14*$^{-/-}$ → WT; n = 5) mice and were implanted with e0771 cells in the mammary fat pad, and tumor growth was monitored.

Graphs represent the average ± SEM. $^{**}p < 0.01$, $^{***}p < 0.001$, $^{****}p < 0.0001$.

above, *Atg14*$^{-/-}$ → WT BMC mice also displayed a dramatic reduction in tumor growth compared to mice that received control *Atg14*$^{+/-}$ bone marrow (Figure 1H). Collectively, these data demonstrate that canonical autophagy suppresses anti-tumor responses against syngeneic tumors.

Atg5 Loss Promotes the Formation of CD8$^+$ T Effector Cells

In line with previous studies demonstrating a loss of peripheral T cells following knockout of autophagy, *Atg5*$^{-/-}$ mice bearing e0771 or Tramp-C2 tumors displayed a significant reduction in CD8$^+$ and CD4$^+$ T cell numbers in peripheral blood and spleen (Figures S2A–S2C). Moreover, e0771 tumors from *Atg5*$^{-/-}$ mice had a decreased number of tumor-infiltrating T cells (TILs) (Figure S2B). This decrease in TILs was also observed in *Atg5*$^{-/-}$ → WT BMCs (Figure S2D). Thus, despite the striking capacity to reject implanted tumors in *Atg5*$^{-/-}$ mice, there was a decrease in the total number of T cells in all compartments that were examined.

To explore the basis of the observed dichotomy of reduced T cell infiltration and increased anti-tumor responses, the patterns of T cell differentiation were examined in greater detail. *Atg5*$^{-/-}$ tumor-bearing mice contained a marked increase in peripheral CD8$^+$ effector memory T cells (CD62L^{lo}CD44^{hi}) (Figures 2A, 2B, and S2E). This shift to effector memory T cells was even more prominent in CD8$^+$ TILs from *Atg5*$^{-/-}$ mice, where more

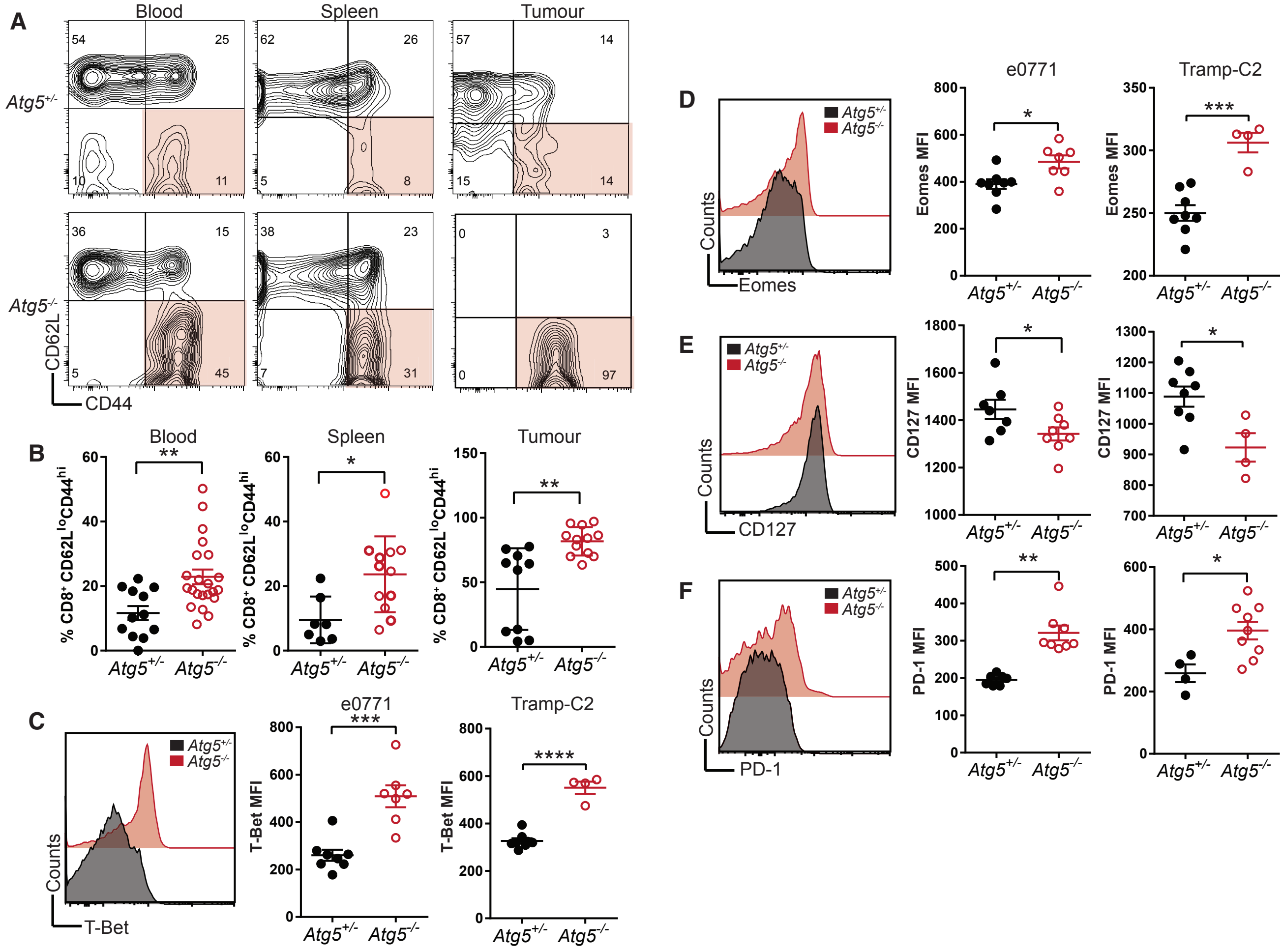

Figure 2. Atg5 Deficiency Leads to Increased Effector Memory CD8$^+$ T Cells

(A) Representative flow cytometry plots showing naive (CD62L^{hi}CD44^{lo}), central memory (CD62L^{hi}CD44^{hi}), and effector memory (CD62L^{lo}CD44^{hi}) CD8$^+$ T cells isolated from blood, spleen, and tumors of e0771 tumor-bearing mice.

(B) Percentages of CD62L^{lo}CD44^{hi} effector memory CD8$^+$ T cells in blood, spleen, and tumors from e0771 tumor-bearing mice.

(C–F) Representative histograms showing (C) T-Bet, (D) Eomes, (E) CD127, and (F) PD-1 expression on CD8$^+$ T cells from *Atg5*$^{+/-}$ (dark gray) and *Atg5*$^{-/-}$ (red) e0771 or Tramp-C2 tumor-bearing mice.

Graphs represent the average mean fluorescence intensity (MFI) ± SEM. $^*p < 0.05$, $^{**}p < 0.01$, $^{***}p < 0.001$, $^{****}p < 0.0001$.

than 80% of the CD8$^+$ TILs exhibited this phenotype (Figures 2A and 2B). A similar pattern of differentiation was also observed in CD8$^+$ T cells from *Atg5*$^{-/-}$ → WT BMC mice (Figure S2F). In addition to changes observed in CD44 and CD62L expression, splenic CD8$^+$ T cells from *Atg5*$^{-/-}$ mice also displayed a significant increase in T-Bet and Eomes (Figures 2C and 2D), transcription factors that are critical for the formation and function of effector CD8$^+$ T cells (Intlekofer et al., 2005; Pearce et al., 2003). Consistent with the higher frequency of T-Bet and Eomes expression, *Atg5*$^{-/-}$ CD8$^+$ T cells had reduced expression of CD127 (IL-7Ra), a marker of central memory T cells (Figure 2E), and a greater proportion of PD-1 positivity, a marker of antigen-experienced T cells (Figure 2F). In contrast to previous findings (Stephenson et al., 2009), no significant difference in the frequency of *Atg5*$^{-/-}$ effector memory CD4$^+$ T cells was found in any of the tissues examined from e0771 or Tramp-C2 tumor-bearing mice (Figures S2G and S2H). These results imply that loss of autophagy shifts the differentiation state of CD8$^+$ T cells to an effector memory phenotype that is unique and intrinsic from the differentiation patterns acquired by CD4$^+$ T cells.

Autophagy Inhibits Secretion of Effector Cytokines

The increased frequency of effector memory T cells suggests that this differentiated state could impart greater anti-tumor function in mice lacking autophagy. Indeed, *ex vivo* phorbol 12-myristate 13-acetate (PMA)/ionomycin stimulation of *Atg5*$^{-/-}$ CD8$^+$ T cells from e0771 or Tramp-C2 tumor-bearing mice led to an increase in production of both IFN-γ and TNF-α (Figure 3A). Moreover, a global elevation in serum IFN-γ levels was observed in *Atg5*$^{-/-}$ e0771 and Tramp-C2 tumor-bearing mice compared to the controls (Figure 3B). These responses were antigen specific as *Atg5*$^{-/-}$ T cells isolated from e0771 or Tramp-C2

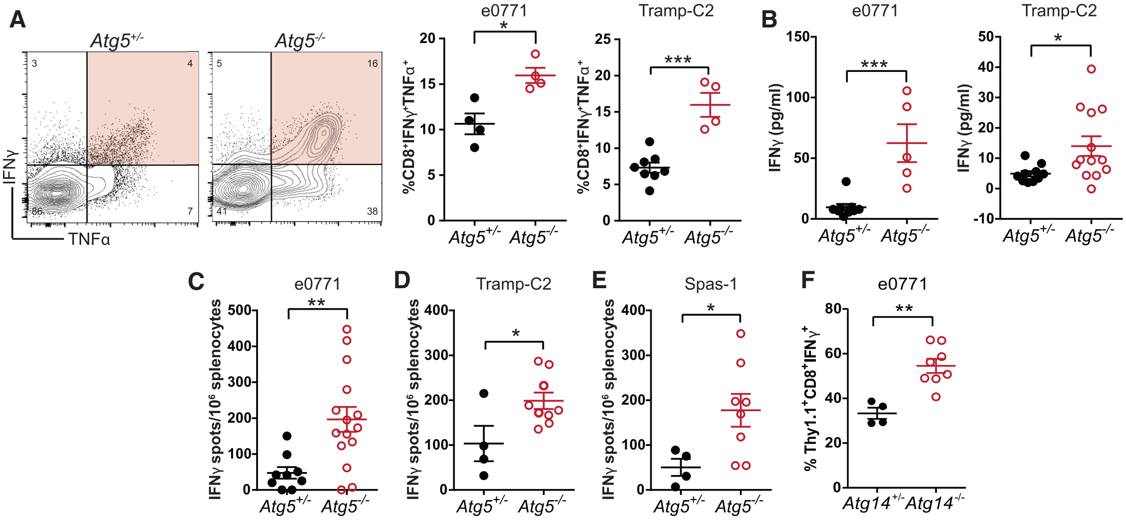

Figure 3. *Atg5$^{-/-}$* CD8$^+$ T Cells Secrete High Levels of Th1 Cytokines

(A) Representative flow cytometry plots showing IFN-γ and TNF-α expression following PMA and ionomycin stimulation of *Atg5$^{+/-}$* and *Atg5$^{-/-}$* CD8$^+$ T cells from Tramp-C2 tumor-bearing mice. Graphs represent the percentage of IFN-γ$^+$TNF-α$^+$ CD8$^+$ T cells in e0771 and Tramp-C2 tumor-bearing mice ± SEM.

(B) Serum from e0771 or Tramp-C2 tumor-bearing mice was analyzed by ELISA.

(C) Splenocytes harvested from *Atg5$^{+/-}$* and *Atg5$^{-/-}$* e0771 tumor-bearing mice were stimulated with e0771 cells, and IFN-γ ELISPOT assays were performed.

(D and E) Splenocytes harvested from Tramp-C2 tumor-bearing mice were stimulated with (D) Tramp-C2 cells or (E) Spas-1 peptide, and IFN-γ ELISPOT assays were performed.

(F) CD8$^+$ TILs from *Atg14$^{+/-}$* or *Atg14$^{-/-}$* BMC mice were harvested and analyzed by flow cytometry for IFN-γ expression.

Graphs represent the average ± SEM. $^*p < 0.05$, $^{**}p < 0.01$, $^{***}p < 0.001$.

tumor-bearing mice secreted higher amounts of IFN-γ against e0771 or Tramp-C2 tumor cells, respectively (Figures 3C and 3D). Moreover, *Atg5$^{-/-}$* T cells from Tramp-C2 tumor-bearing mice secreted higher levels of IFN-γ in response to the Tramp-C2 mutant peptide Spas1 (Figure 3E). Consistent with these observations, CD8$^+$ TILs from donor *Atg14$^{-/-}$* → WT BMC mice produced elevated levels of IFN-γ compared to CD8$^+$ TILs from the donor *Atg14$^{+/-}$* → WT BMC mice (Figure 3F).

CD8$^+$-Dependent and T-Cell-Specific Loss of Atg5 Enhances Tumor Rejection

To further investigate the requirement of T cells in promoting tumor rejection following deletion of Atg5, CD8$^+$ T cells were selectively depleted from *Atg5$^{-/-}$* mice with an anti-CD8 antibody. In contrast to isotype controls, there was a complete restoration of tumor growth in animals treated with anti-CD8-depleting antibodies (Figure 4A). Analysis of cytokine mRNA expression was examined in tumors following CD8$^+$ T cell depletion. Tumors from isotype-control-treated *Atg5$^{-/-}$* mice had a significant increase in *Ifng* expression that was completely abrogated upon CD8$^+$ T cell depletion (Figure 4B). No significant change in other Th1 (*Tnf* and *Il2*) or Th2 (*Il4*, *Il6*, and *Il10*) cytokines was observed (Figures S3A–S3E).

Mixed BMCs were generated to determine the T cell-intrinsic role for autophagy in mediating tumor regression. Reconstitution of mice with bone marrow (BM) from WT (Thy1.2$^+$) mice, mixed 1:1 with BM from *Atg5$^{-/-}$* or *Atg5$^{+/-}$* Thy1.1$^+$ donor mice, also resulted in a reduction in tumor growth (Figure 4C). Importantly, no significant difference in the ratio of Thy1.1$^+$CD8$^+$ to Thy1.2$^+$ Tregs was observed in the mixed BMCs, indicating that deletion of *Atg5* does not alter self-tolerance in this model (Figure S4A). To further determine whether CD8$^+$ T cell autophagy could mediate tumor control, *Atg5$^{-/-}$* OTI T cells were adoptively transferred into mice that were previously implanted with EL4-OVA tumor cells. In contrast to mice receiving a subtherapeutic dose of control *Atg5$^{+/-}$* OTI T cells, where tumors progressively increased in size, a single adoptive cell transfer of *Atg5$^{-/-}$* OTI T cells resulted in tumor control (Figures 4D and 4E). Consistent with the observed anti-tumor response, *Atg5$^{-/-}$* OTI T cells from the tumor draining lymph node and spleens secreted a higher amount of IFN-γ than those from mice that received control *Atg5$^{+/-}$* OTI T cells (Figures 4F and 4G).

Autophagy Suppresses Glucose Utilization in CD8$^+$ T Cells

To explore the mechanisms by which loss of autophagy enhances anti-tumor activity of CD8$^+$ T cells, metabolomic profiling was performed on *Atg5*-deficient CD8$^+$ T cells isolated from e0771 tumor-bearing mice. A total of 94 metabolites were identified, of which 54 were significantly altered in *Atg5$^{-/-}$* CD8$^+$ T cells compared to *Atg5$^{+/-}$* CD8$^+$ T cells ($p < 0.05$) (Figure 5A). The metabolites are shown in the volcano plot in Figure 5B (black dots) in relation to all others (gray dots, $p > 0.05$) and include both significantly upregulated and downregulated metabolites. A pathway enrichment analysis was performed to identify key pathways altered in *Atg5$^{-/-}$* CD8$^+$ T cells. The top five enriched pathways included purine, betaine, glutamate, arginine and proline, and methionine metabolism (Figure 5C).

The metabolomics data revealed that *Atg5$^{-/-}$* CD8$^+$ T cells had a marked increase in the glycolytic metabolite lactate

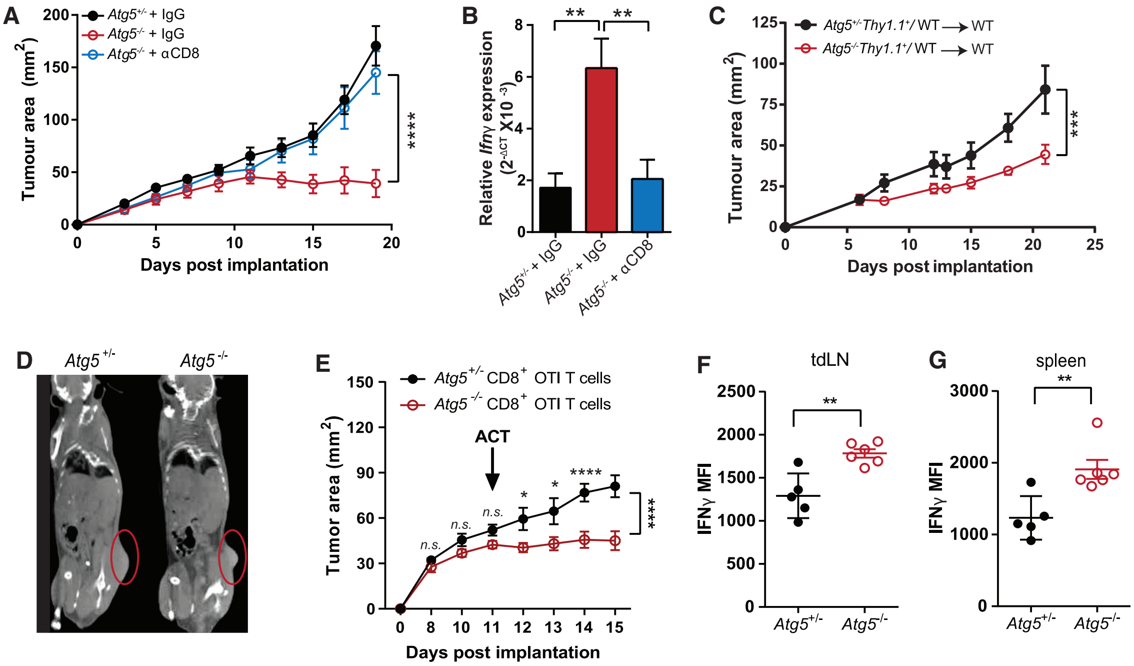

Figure 4. *Atg5*$^{-/-}$ CD8^{+} T Cells Are Required to Control Tumor Growth

(A) *Atg5*$^{-/-}$ mice were treated with a CD8-depleting antibody or an immunoglobulin G (IgG) isotype control prior to e0771 tumor cell implantation. *Atg5*$^{+/-}$ mice treated with an IgG isotype antibody were used as a control. Data are expressed as average ± SEM.

(B) Relative expression of *IFN*γ was measured from tumors harvested in (A).

(C) Lethally irradiated WT mice received BM from *Atg5*$^{+/-}$ or *Atg5*$^{-/-}$ Thy1.1^{+} mice mixed 1:1 with WT BM (Thy1.2^{+}). Data are expressed as average ± SEM.

(D) Computed tomography (CT) scan on day 15 post-implantation of EL4-OVA tumor cells following adoptive transfer of 1 × 10^{6} *Atg5*$^{+/-}$ or *Atg5*$^{-/-}$ OTI T cells at day 11.

(E) Tumor growth was monitored in mice that received adoptive cell transfer (ACT) from (D). Data are expressed as average ± SEM.

(F and G) IFN-γ production from CD8^{+} T cells isolated from tumor draining lymph nodes (F) and spleens (G) of mice in (D) following *in vitro* PMA/ionomycin stimulation.

Graphs represent average MFI ± SEM. **$p < 0.01$, ****$p < 0.0001$, *n.s.*, not significant.

(Figures 5A, 5B, and 5D). To examine if the changes in lactate reflected functional differences in glucose metabolism, the oxygen consumption rate (OCR), an indicator of mitochondrial respiration, and the extracellular acidification rate (ECAR), an indicator of glycolysis, were measured in T cells from tumor-bearing *Atg5*$^{+/-}$ and *Atg5*$^{-/-}$ mice. In the basal state, *Atg5*$^{-/-}$ CD8^{+} T cells displayed an elevated OCR and ECAR compared to *Atg5*$^{+/-}$ CD8^{+} T cells (Figures 5E–5G). However, *Atg5*$^{-/-}$ CD8^{+} T cells had a significant reduction in the OCR:ECAR ratio, indicating that *Atg5*$^{-/-}$ CD8^{+} T cells shift to a more glycolytic state (Figure 5H). Consistent with the observed increase in glycolysis, both *Atg5*$^{-/-}$ CD8^{+} T cells and T cells from *Atg14*$^{-/-}$ → WT BMC mice displayed enhanced uptake of the fluorescent glucose analog 2-NBDG (Figures 5I–5L). Mitochondrial activity, including the spare respiratory capacity and mitochondrial mass, were comparable between the *Atg5*$^{-/-}$ and *Atg5*$^{+/-}$ CD8^{+} T cells (Figures 5M and 5N).

Increased H3K4me3 in the Absence of *Atg5*

The metabolomics analysis revealed that *Atg5*$^{-/-}$ CD8^{+} T cells had a significant decrease in SAM, while no significant difference in methionine was observed in *Atg5*$^{+/-}$ and *Atg5*$^{-/-}$ CD8^{+} T cell subsets (Figure S5A). SAM is a ubiquitous methyl donor for methylation modifications on substrates including DNA and histones. SAM is synthesized from ATP and methionine in the methionine cycle. The change in SAM prompted an examination of whether epigenetic modifications might explain the dramatic changes in T cell differentiation and metabolism in the absence of *Atg5*. Indeed, *Atg5*$^{-/-}$ CD8^{+} T cells showed a reduction in the global level of histone H3K27 trimethylation (H3K27me3), a mark for inactive gene promoters, compared to controls (Figures S5B and S5C). To examine whether this broad decrease in H3K27me3 could affect local enrichment and expression of metabolic and effector genes, H3K27me3 and H3K4me3 (an activating mark) chromatin immunoprecipitation sequencing (ChIP-seq) was performed on CD8^{+} TILs from *Atg5*$^{+/-}$ and *Atg5*$^{-/-}$. ChIP-seq confirmed a reduction in H3K27me3 signal coverage with few localized differences in *Atg5*$^{+/-}$ and *Atg5*$^{-/-}$ CD8^{+} TILs (Figures S5D, S5E, and S5G). Assessment of promoters in protein coding genes identified 11670 and 11243 H3K4me3 enriched promoters (±2 kb of the transcription start site) in *Atg5*$^{-/-}$ and *Atg5*$^{+/-}$ TILs, respectively. Of these, 466 promoters were uniquely enriched in *Atg5*$^{-/-}$ cells compared to 39 uniquely enriched promoters in *Atg5*$^{+/-}$ cells. Strikingly, pathway and gene ontology analysis of H3K4me3-marked genes unique to the

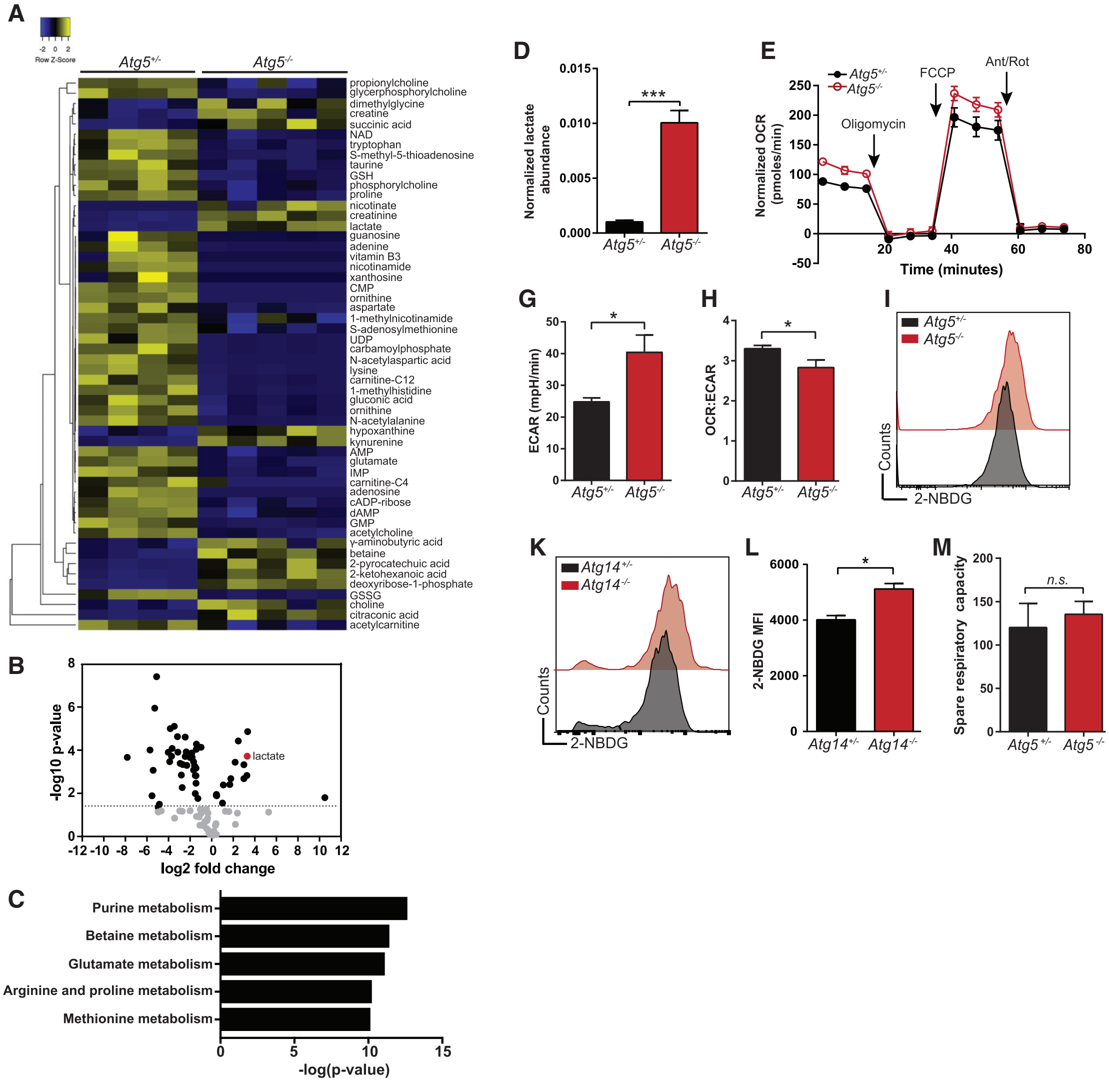

Figure 5. Metabolite Changes in *Atg5*$^{-/-}$ CD8$^+$ T Cells

(A) A heatmap demonstrating significantly altered metabolites in *Atg5*$^{-/-}$ CD8$^+$ T cells compared to *Atg5*$^{+/-}$ CD8$^+$ T cells using hierarchical clustering of normalized signal intensities ($\log_2$ transformed and row adjusted). Blue indicates low expression, while yellow indicates high expression of the detected metabolites.

(B) A volcano plot of metabolites from *Atg5*$^{+/-}$ and *Atg5*$^{-/-}$ CD8$^+$ T cells showing $\log_2$ fold change and $-\log_{10}$ p value. A $-\log_{10}$ p value > 1.3 (black dots) was considered statistically significant. All others are shown in gray; lactate is shown in red.

(C) Metabolites significantly altered ($p < 0.05$) in *Atg5*$^{-/-}$ CD8$^+$ T cells compared to *Atg5*$^{+/-}$ CD8$^+$ T cells were subjected to MetaboAnalyst for pathway enrichment analysis. The top-five enriched pathways are shown ($p < 0.001$).

(D) Relative lactate levels identified by metabolomics. Error bars indicate ± SD.

(E–H) CD8$^+$ T cells were isolated from spleens of e0771 tumor-bearing mice and subjected to Seahorse Bioanalyzer in the presence or absence of oligomycin, carbonyl cyanide-4-(trifluoromethoxy)phenylhydrazone (FCCP), and antimycin and rotenone (Ant/Rot) (E). Data were normalized to protein concentration. Error bars indicate ± SEM (F) OCR, (G) ECAR, and (H) OCR:ECAR ratio of *Atg5*$^{+/-}$ and *Atg5*$^{-/-}$ CD8$^+$ T cells was examined at basal levels.

(I and J) Representative flow cytometry plot showing 2-NBDG uptake in splenic *Atg5*$^{+/-}$ (dark gray) and *Atg5*$^{-/-}$ (red) CD8$^+$ T cells from e0771 tumor-bearing mice (I). Graph represents the MFI of 2-NBDG ± SEM (J).

(K and L) Representative flow cytometry plot showing 2-NBDG uptake in splenic *Atg14*$^{+/-}$ (dark gray) and *Atg14*$^{-/-}$ (red) CD8$^+$ T cells from e0771 tumor-bearing mice (K). Graph represents the MFI of 2-NBDG ± SEM (L).

(M and N) Spare respiratory capacity, indicated by baseline OCR subtracted from maximal OCR (M), and mitochondrial mass as measured by MitoTracker Green, was determined in *Atg5*$^{+/-}$ and *Atg5*$^{-/-}$ CD8$^+$ T cells isolated from e0771 tumor-bearing mice (N).

Graphs represent average ± SEM; n = 4–5 mice per group. *$p < 0.05$, **$p < 0.01$, ***$p < 0.001$; *n.s.*, not significant.

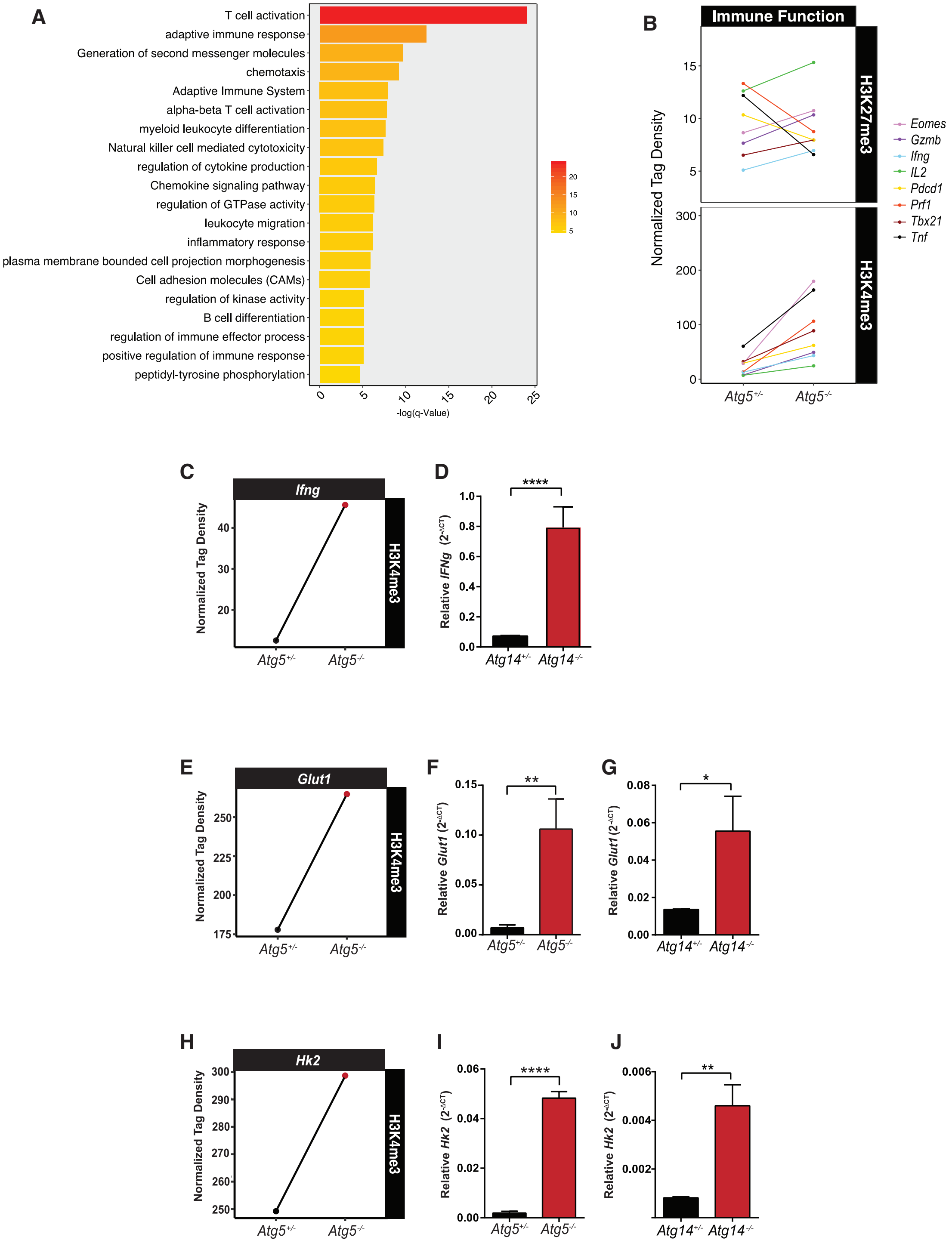

Figure 6. Histone Tri-methylation Changes in *Atg5*$^{-/-}$ CD8^{+} T Cells from e0771 Tumors

(A) Pathway and gene ontology analysis of H3K4me3-marked promoters unique to *Atg5*$^{-/-}$ versus *Atg5*$^{+/-}$ CD8^{+} T cells are strongly enriched in genes related to T cell activation and adaptive immunity (Benjamini q value < 10e-12).

(B) Differential normalized tagged density of H3K27me3 and H3K4me3 in a subset of immune response genes.

(C and D) ChIP-seq on *Atg5*$^{+/-}$ and *Atg5*$^{-/-}$ CD8^{+} T cells for H3K4me3 for *Ifng.* (C) Normalized tag density of *Ifng* in knockout or control CD8^{+} T cells. (D) qRT-PCR of *Ifng* expression in *Atg14*$^{+/-}$ and *Atg14*$^{-/-}$ CD8^{+} T cells. Results are relative to *Actb.* Data are expressed as average ± SEM of a triplicate experiment with at least 2 mice per group.

(legend continued on next page)

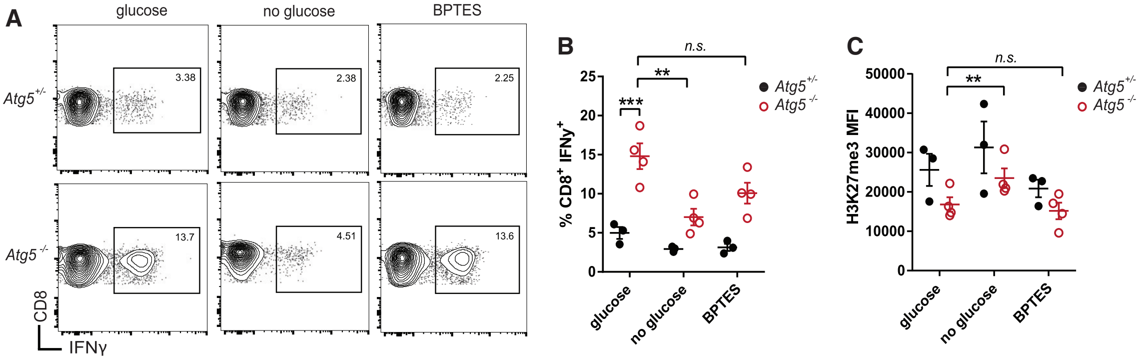

Figure 7. Glucose Deprivation Inhibits the Upregulation of IFN-γ in the Absence of *Atg5*

(A) Representative flow cytometry plots showing IFN-γ production following PMA and ionomycin stimulation of splenic *Atg5*$^{+/-}$ and *Atg5*$^{-/-}$ CD8$^+$ T cells from Tramp-C2 tumor-bearing mice. Cells were cultured in full media, media without glucose, or media with glucose in the presence of 10 μM BPTES.

(B) Graphs represent the percentage of CD8$^+$ IFN-γ$^+$ T cells cultured in the presence or absence of glucose or with BPTES treatment.

(C) Graphs represent H3K27me3 mean fluorescence intensity in CD8$^+$ T cells cultured in the presence or absence of glucose or with BPTES treatment.

$^{**}p < 0.01$, $^{***}p < 0.001$, *n.s.*, not significant.

Atg5$^{-/-}$ TILs revealed significant enrichment for genes involved in T cell activation and immune responses (Figures 6A and S5F). In line with our immune phenotyping, *Atg5*$^{-/-}$ T cells displayed an increase in H3K4me3 at the *Eomes*, *Gzmb*, *Ifng*, *IL-2*, *Pdcd1*, *Prf1*, *Tbx21*, and *Tnf* loci (Figures 6B, 6C, and S5F; Araki et al., 2009). The increase in H3K4me3 density at the *Ifng* locus correlated with increased mRNA expression (Figure 6D). Although metabolic genes as a group were not identified as enriched or uniquely marked by H3K4me3 in *Atg5*$^{-/-}$ TILs, an increase in H3K4me3 density was apparent in the promoters of key glycolytic genes, albeit less than the observed changes for immune related genes. These included the glucose transporter *Glut1* (*Slc2a1*) (Figure 6E), hexokinase 2 (*Hk2*) (Figures 6H), lactate dehydrogenase (*Ldhb*), and pyruvate kinase (*Pkm*) (Figure S5H), all of which showed an increase in H3K4me3 promoter density in *Atg5*$^{-/-}$ compared to *Atg5*$^{+/-}$ TILs. In agreement with an increase in H3K4me3 density, both *Atg5*$^{-/-}$ and *Atg14*$^{-/-}$ T cells had increased mRNA expression of *Glut1* and *Hk2* (Figures 6F, 6G, 6I, and 6J). Collectively, these observations are consistent with a model whereby global loss of H3K27me3 permitted specific gains of H3K4me3 and enabled the activation of a glycolytic transcriptional program in *Atg5*$^{-/-}$ T cells.

Glucose Restriction Reverses Autophagy-Dependent Suppression of IFN-γ

To determine whether changes in glucose uptake are important for regulating effector function, T cells from *Atg5*$^{+/-}$ or *Atg5*$^{-/-}$ mice were cultured in the presence or absence of glucose. In the presence of glucose, deletion of *Atg5*$^{-/-}$ resulted in higher T cell secretion of IFN-γ compared to *Atg5*$^{+/-}$ CD8$^+$ T cells. Following short-term glucose starvation, there was a 3-fold reduction in IFN-γ production in *Atg5*$^{-/-}$ CD8$^+$ T cells, whereas no change in IFN-γ was observed in *Atg5*$^{+/-}$ CD8$^+$ T cells irrespective of whether glucose was present (Figures 7A and 7B). Accordingly, glucose restriction reversed the global decrease in H3K27me3 observed in *Atg5*$^{-/-}$ T cells (Figure 7C). No difference in the secretion of IFN-γ or levels of histone trimethylation was observed in either *Atg5*$^{-/-}$ or *Atg5*$^{+/-}$ CD8$^+$ T cells treated with bis-2-(5-phenylacetamido-1,3,4-thiadiazol-2-yl)ethyl sulfide (BPTES), a selective glutaminase inhibitor, suggesting a requirement for glucose metabolism but not oxidative metabolism in the regulation of effector cytokine production.

DISCUSSION

Emerging evidence indicates that autophagy may play a role in immunosurveillance; however, the role of autophagy in tumor growth and anti-tumor immune responses is still not completely understood. While it has been demonstrated that Beclin1 acts as a tumor suppressor (Qu et al., 2003), deletion of other autophagy genes, including *FIP200*, *Atg5*, and *Atg7*, not only reduced tumor growth but also, in some cases, altered anti-tumor immune responses (Lévy et al., 2015; Rao et al., 2014; Salah et al., 2016; Wei et al., 2016). Although chloroquine treatment did not impact T cell responses in tumor-bearing mice (Starobinets et al., 2016), we demonstrate that genetic deletion of *Atg5* enhances CD8$^+$ T cell-intrinsic effector activity, resulting in rejection of transplanted tumors. The discrepancy between pharmacological and genetic inhibition of autophagy could be attributed to the

---

(E–G) ChIP-seq on *Atg5*$^{+/-}$ and *Atg5*$^{-/-}$ CD8$^+$ T cells for H3K4me3 for *Glut1*. (E) Normalized tag density of *Glut1* in knockout or control CD8$^+$ T cells. (F) qRT-PCR of *Glut1* expression in *Atg5*$^{+/-}$ and *Atg5*$^{-/-}$ CD8$^+$ T cells or (G) *Atg14*$^{+/-}$ and *Atg14*$^{-/-}$ CD8$^+$ T cells. Results are relative to *Actb.* Data are expressed as average ± SEM of a triplicate experiment with at least 2 mice per group.

(H–J) ChIP-seq on *Atg5*$^{+/-}$ and *Atg5*$^{-/-}$ CD8$^+$ T cells for H3K4me3 for *Hk2.* (H) Normalized tag density of *Hk2* in knockout or control CD8$^+$ T cells. (I) qRT-PCR of *Hk2* expression in *Atg5*$^{+/-}$ and *Atg5*$^{-/-}$ CD8$^+$ T cells or (J) *Atg14*$^{+/-}$ and *Atg14*$^{-/-}$ CD8$^+$ T cells. Results are relative to *Actb.* Data are expressed as average ± SEM of a triplicate experiment with at least 2–3 mice per group.

$^{*}p < 0.01$, $^{**}p < 0.01$, $^{****}p < 0.001$, *n.s.*, not significant.

timing and duration of chloroquine treatment or the fact that chloroquine is a lysomotropic agent that blocks late-stage autophagy. Moreover, although Atg5 has functions independent of autophagy, including roles in apoptosis (Yousefi et al., 2006) and mitotic catastrophe (Maskey et al., 2013), our findings with genetic ablation of *Atg16L1* and *Atg14*$^{-/-}$ BMC mice show that these effects are dependent on canonical autophagy and not strictly dependent on Atg5.

Following activation, T cells undergo dramatic metabolic reprogramming to support growth, proliferation, and activation of cytotoxic effector programs. T cells integrate signals from the microenvironment to coordinate the necessary metabolic programs to initiate and support effector functions. Specifically, T effector cells display increased glycolysis, while activated CD8$^+$ T cells with a lower bioenergetic OXPHOS and glycolytic profile are more permissive to form memory (Chang et al., 2013; Sukumar et al., 2013). Despite using aerobic glycolysis, most activated T cells also consume oxygen, indicating that both OXPHOS and glycolysis can run in parallel (Cao et al., 2014; Wang et al., 2011). Our results demonstrate an important role for autophagy in restraining glycolytic metabolism and effector functions in CD8$^+$ T cells. CD8$^+$ T cells deleted of *Atg5* acquired an effector memory phenotype associated with increased IFN-γ and TNF-α production. This resulted in both *Atg5*- and *Atg14*-dependent increases in glucose metabolism. When *Atg5*$^{-/-}$ T cells were restricted of glucose, the production of IFN-γ was reduced to levels similar to *Atg5*$^{+/-}$ T cells, implying an *Atg5*-dependent regulation of glucose metabolism in controlling CD8$^+$ T effector function. Recent data suggest that Treg-specific deletion of *Atg5* or *Atg7* breaks self-tolerance, resulting in an acquisition of an effector memory phenotype in both CD8$^+$ and CD4$^+$ T cells (Wei et al., 2016). In our model, however, no significant changes in the CD4$^+$ T cell effector memory compartment were observed, nor was there any major difference in the ratio of CD8$^+$ T cells to Tregs in the absence of *Atg5*. Moreover, the current study does not conflict or rule out additional autophagy-related functions such as LC3-associated phagocytosis on other immune subsets, including myeloid cells and their roles in regulation immune suppression of T cells (Cunha et al., 2018). Indeed, these collective studies are not surprising given the inherent functional differences between T cells and myeloid cells in the tumor microenvironment that further highlight the complex interactions between immune cells to coordinate immune-mediated rejection of tumors.

Recent studies in tumor cells have identified a number of key metabolites that are involved in the regulation of enzymes responsible for histone modifications (Wong et al., 2017). In T cells, however, the link between metabolism and epigenetic regulation remains understudied. It has been demonstrated that alterations in histone methylation occur in response to changes in SAM and S-adenosylhomocysteine (SAH) (Mentch et al., 2015). Consistent with these reports and the data presented here demonstrating a reduction in SAM levels in *Atg5*$^{-/-}$ TILs, we observed a global loss of H3K27me3 and concurrent gains of H3K4me3. H3K27me3 is a key repressive epigenetic modification implicated in hematopoietic lineage fate decisions, and its global loss would be expected to associate with the activation of a cell-context-specific transcription program (Zhang et al., 2012). Supporting this concept, we observed local gains in H3K4me3, a mark that acts in opposition and is mutually exclusive with H3K27me3 at active gene promoters (Bernstein et al., 2006). Thus, our results demonstrate that changes in glycolytic metabolism due to the loss of autophagy promote an enhanced T cell transcriptional program. It is possible that the increase in glucose-derived lactate observed in *Atg5*$^{-/-}$ T cells indicates a reduction in carbon available for methylation reactions, ultimately resulting in global and specific epigenetic alterations.

Emerging evidence from cancer immunotherapy clinical trials have highlighted an important role for T cells in mediating the elimination of tumors. While the results of immunotherapies have been encouraging in the context of hematological cancers and more recently in melanoma, targeting other solid cancers has been largely unsuccessful. Several factors, including metabolic competition in the tumor microenvironment, could suppress T cell function following infusion. Consistent with this, in murine tumors, glucose consumption by tumors metabolically restricts T cells, leading to reduced IFN-γ production and increased tumor progression (Chang et al., 2015). However, as shown in this study, deletion of T cell autophagy may shift the metabolic advantage for these nutrients back in favor of T cells, a strategy that could be used to enhance immunotherapy against human cancers.

STAR★METHODS

Detailed methods are provided in the online version of this paper and include the following:

- KEY RESOURCES TABLE
- CONTACT FOR REAGENT AND RESOURCE SHARING
- EXPERIMENTAL MODEL AND SUBJECT DETAILS
  - Mice
  - Cell culture
- METHOD DETAILS
  - Tumor challenge
  - Immunohistochemistry
  - Western blotting
  - IFNγ ELISPOT and ELISA
  - T cell stimulation
  - Flow cytometry
  - Quantitative RT-PCR
  - Metabolism assays
  - Metabolomics
  - Low input native ChIP-Seq
- QUANTIFICATION AND STATISTICAL ANALYSIS
- DATA AND SOFTWARE AVAILABILITY

SUPPLEMENTAL INFORMATION

Supplemental Information can be found online at https://doi.org/10.1016/j.celrep.2019.03.037.

ACKNOWLEDGMENTS

The authors would like to thank Chris Johnstone and Dr. Magdalena Bazalova-Carter for assistance with radiation of mice to create the bone marrow chimeras, Dr. John Stagg for the e0771 cells, and Dr. Ravi Amaravadi for

Lys05. This study was supported by the Canadian Breast Cancer Foundation (J.J.L.), the BC Cancer Foundation (J.J.L.), the Canadian Breast Cancer Foundation Fellowship (L.D.), the Howard Hughes Medical Institute (Faculty Scholars Program; R.J.D.), and the National Cancer Institute (1R35CA22044901; R.J.D.).

AUTHOR CONTRIBUTIONS

Conceptualization, L.D. and J.J.L.; Methodology, L.D., N.P., M.H., A.M., and J.J.L.; Investigation, L.D., N.P., G.C., A.C., C.H., P.K., J.L., E.M, H.H, L.G.Z., N.M., T.S., S.A., W.B., A.L., M.M., and Q.C.; Writing – Original Draft and Revisions, all authors; Visualization, L.D., A.C., and J.J.L., Supervision, L.D, A.M., M.H., and J.J.L., Funding Acquisition, L.D and J.J.L.

DECLARATION OF INTERESTS

R.J.D. is member of the Scientific Advisory Board at Agios Pharmaceuticals. A.M., J.L., E.M., and H.H. are employees of Genentech Inc. L.D. and J.J.L. are named inventors on a provisional patent related to the research in this manuscript.

Received: March 6, 2018
Revised: February 14, 2019
Accepted: March 8, 2019
Published: April 9, 2019

REFERENCES

Araki, Y., Wang, Z., Zang, C., Wood, W.H., 3rd, Schones, D., Cui, K., Roh, T.-Y., Lhotsky, B., Wersto, R.P., Peng, W., et al. (2009). Genome-wide analysis of histone methylation reveals chromatin state-based regulation of gene transcription and function of memory CD8+ T cells. Immunity *30*, 912–925.

Bernstein, B.E., Mikkelsen, T.S., Xie, X., Kamal, M., Huebert, D.J., Cuff, J., Fry, B., Meissner, A., Wernig, M., Plath, K., et al. (2006). A bivalent chromatin structure marks key developmental genes in embryonic stem cells. Cell *125*, 315–326.

Buck, M.D., O'Sullivan, D., and Pearce, E.L. (2015). T cell metabolism drives immunity. J. Exp. Med. *212*, 1345–1360.

Cao, Y., Rathmell, J.C., and Macintyre, A.N. (2014). Metabolic reprogramming towards aerobic glycolysis correlates with greater proliferative ability and resistance to metabolic inhibition in CD8 versus CD4 T cells. PLoS One *9*, e104104.

Chang, C.-H., Curtis, J.D., Maggi, L.B., Jr., Faubert, B., Villarino, A.V., O'Sullivan, D., Huang, S.C.-C., van der Windt, G.J.W., Blagih, J., Qiu, J., et al. (2013). Posttranscriptional control of T cell effector function by aerobic glycolysis. Cell *153*, 1239–1251.

Chang, C.-H., Qiu, J., O'Sullivan, D., Buck, M.D., Noguchi, T., Curtis, J.D., Chen, Q., Gindin, M., Gubin, M.M., van der Windt, G.J.W., et al. (2015). Metabolic competition in the tumor microenvironment is a driver of cancer progression. Cell *162*, 1229–1241.

Cunha, L.D., Yang, M., Carter, R., Guy, C., Harris, L., Crawford, J.C., Quarato, G., Boada-Romero, E., Kalkavan, H., Johnson, M.D.L., et al. (2018). LC3-associated phagocytosis in myeloid cells promotes tumor immune tolerance. Cell *175*, 429–441.e16.

Feng, J., Liu, T., Qin, B., Zhang, Y., and Liu, X.S. (2012). Identifying ChIP-seq enrichment using MACS. Nat. Protoc. *7*, 1728–1740.

Hara, T., Nakamura, K., Matsui, M., Yamamoto, A., Nakahara, Y., Suzuki-Migishima, R., Yokoyama, M., Mishima, K., Saito, I., Okano, H., and Mizushima, N. (2006). Suppression of basal autophagy in neural cells causes neurodegenerative disease in mice. Nature *441*, 885–889.

Heinz, S., Benner, C., Spann, N., Bertolino, E., Lin, Y.C., Laslo, P., Cheng, J.X., Murre, C., Singh, H., and Glass, C.K. (2010). Simple combinations of lineage-determining transcription factors prime cis-regulatory elements required for macrophage and B cell identities. Mol. Cell *38*, 576–589.

Hubbard, V.M., Valdor, R., Patel, B., Singh, R., Cuervo, A.M., and Macian, F. (2010). Macroautophagy regulates energy metabolism during effector T cell activation. J. Immunol. *185*, 7349–7357.

Intlekofer, A.M., Takemoto, N., Wherry, E.J., Longworth, S.A., Northrup, J.T., Palanivel, V.R., Mullen, A.C., Gasink, C.R., Kaech, S.M., Miller, J.D., et al. (2005). Effector and memory CD8+ T cell fate coupled by T-bet and eomesodermin. Nat. Immunol. *6*, 1236–1244.

Itakura, E., Kishi, C., Inoue, K., and Mizushima, N. (2008). Beclin 1 forms two distinct phosphatidylinositol 3-kinase complexes with mammalian Atg14 and UVRAG. Mol. Biol. Cell *19*, 5360–5372.

Jia, W., Pua, H.H., Li, Q.-J., and He, Y.-W. (2011). Autophagy regulates endoplasmic reticulum homeostasis and calcium mobilization in T lymphocytes. J. Immunol. *186*, 1564–1574.

Kaizuka, T., and Mizushima, N. (2015). Atg13 is essential for autophagy and cardiac development in mice. Mol. Cell. Biol. *36*, 585–595.

Kimura, H., Hayashi-Takanaka, Y., Goto, Y., Takizawa, N., and Nozaki, N. (2008). The organization of histone H3 modifications as revealed by a panel of specific monoclonal antibodies. Cell Struct. Funct. *33*, 61–73.

Lévy, J., Cacheux, W., Bara, M.A., L'Hermitte, A., Lepage, P., Fraudeau, M., Trentesaux, C., Lemarchand, J., Durand, A., Crain, A.-M., et al. (2015). Intestinal inhibition of Atg7 prevents tumour initiation through a microbiome-influenced immune response and suppresses tumour growth. Nat. Cell Biol. *17*, 1062–1073.

Li, C., Capan, E., Zhao, Y., Zhao, J., Stolz, D., Watkins, S.C., Jin, S., and Lu, B. (2006). Autophagy is induced in CD4+ T cells and important for the growth factor-withdrawal cell death. J. Immunol. *177*, 5163–5168.

Li, H., and Durbin, R. (2010). Fast and accurate long-read alignment with Burrows-Wheeler transform. Bioinformatics *26*, 589–595.

Li, H., Handsaker, B., Wysoker, A., Fennell, T., Ruan, J., Homer, N., Marth, G., Abecasis, G., and Durbin, R.; 1000 Genome Project Data Processing Subgroup (2009). The Sequence Alignment/Map format and SAMtools. Bioinformatics *25*, 2078–2079.

Lorzadeh, A., Bilenky, M., Hammond, C., Knapp, D.J.H.F., Li, L., Miller, P.H., Carles, A., Heravi-Moussavi, A., Gakkhar, S., Moksa, M., et al. (2016). Nucleosome density ChIP-seq identifies distinct chromatin modification signatures associated with MNase accessibility. Cell Rep. *17*, 2112–2124.

Lorzadeh, A., Lopez Gutierrez, R., Jackson, L., Moksa, M., and Hirst, M. (2017). Generation of Native Chromatin Immunoprecipitation Sequencing Libraries for Nucleosome Density Analysis. J. Vis. Exp. *2017*, 56085.

Lu, Q., Yokoyama, C.C., Williams, J.W., Baldridge, M.T., Jin, X., DesRochers, B., Bricker, T., Wilen, C.B., Bagaitkar, J., Loginicheva, E., et al. (2016). Homeostatic control of innate lung inflammation by vici syndrome gene epg5 and additional autophagy genes promotes influenza pathogenesis. Cell Host Microbe *19*, 102–113.

Lum, J.J., DeBerardinis, R.J., and Thompson, C.B. (2005). Autophagy in metazoans: cell survival in the land of plenty. Nat. Rev. Mol. Cell Biol. *6*, 439–448.

MacPherson, S., Horkoff, M., Gravel, C., Hoffmann, T., Zuber, J., and Lum, J.J. (2017). STAT3 Regulation of Citrate Synthase Is Essential during the Initiation of Lymphocyte Cell Growth. Cell Rep. *19*, 910–918.

Maskey, D., Yousefi, S., Schmid, I., Zlobec, I., Perren, A., Friis, R., and Simon, H.-U. (2013). ATG5 is induced by DNA-damaging agents and promotes mitotic catastrophe independent of autophagy. Nat. Commun. *4*, 2130.

Matsunaga, K., Saitoh, T., Tabata, K., Omori, H., Satoh, T., Kurotori, N., Maejima, I., Shirahama-Noda, K., Ichimura, T., Isobe, T., et al. (2009). Two Beclin 1-binding proteins, Atg14L and Rubicon, reciprocally regulate autophagy at different stages. Nat. Cell Biol. *11*, 385–396.

Mentch, S.J., Mehrmohamadi, M., Huang, L., Liu, X., Gupta, D., Mattocks, D., Gómez Padilla, P., Ables, G., Bamman, M.M., Thalacker-Mercer, A.E., et al. (2015). Histone methylation dynamics and gene regulation occur through the sensing of one-carbon metabolism. Cell Metab. *22*, 861–873.

Mullen, A.R., Hu, Z., Shi, X., Jiang, L., Boroughs, L.K., Kovacs, Z., Boriack, R., Rakheja, D., Sullivan, L.B., Linehan, W.M., et al. (2014). Oxidation of alpha-ketoglutarate is required for reductive carboxylation in cancer cells with mitochondrial defects. Cell Rep. *7*, 1679–1690.

Nishimura, T., Kaizuka, T., Cadwell, K., Sahani, M.H., Saitoh, T., Akira, S., Virgin, H.W., and Mizushima, N. (2013). FIP200 regulates targeting of Atg16L1 to the isolation membrane. EMBO Rep. *14*, 284–291.

Park, S., Buck, M.D., Desai, C., Zhang, X., Loginicheva, E., Martinez, J., Freeman, M.L., Saitoh, T., Akira, S., Guan, J.-L., et al. (2016). Autophagy genes enhance murine gammaherpesvirus 68 reactivation from latency by preventing virus-induced systemic inflammation. Cell Host Microbe *19*, 91–101.

Pearce, E.L., Mullen, A.C., Martins, G.A., Krawczyk, C.M., Hutchins, A.S., Zediak, V.P., Banica, M., DiCioccio, C.B., Gross, D.A., Mao, C.-A., et al. (2003). Control of effector CD8+ T cell function by the transcription factor Eomesodermin. Science *302*, 1041–1043.

Pua, H.H., Guo, J., Komatsu, M., and He, Y.-W. (2009). Autophagy is essential for mitochondrial clearance in mature T lymphocytes. J. Immunol. *182*, 4046–4055.

Puleston, D.J., Zhang, H., Powell, T.J., Lipina, E., Sims, S., Panse, I., Watson, A.S., Cerundolo, V., Townsend, A.R., Klenerman, P., and Simon, A.K. (2014). Autophagy is a critical regulator of memory CD8(+) T cell formation. eLife *3*, e03706.

Qu, X., Yu, J., Bhagat, G., Furuya, N., Hibshoosh, H., Troxel, A., Rosen, J., Eskelinen, E.-L., Mizushima, N., Ohsumi, Y., et al. (2003). Promotion of tumorigenesis by heterozygous disruption of the beclin 1 autophagy gene. J. Clin. Invest. *112*, 1809–1820.

Quinlan, A.R., and Hall, I.M. (2010). BEDTools: a flexible suite of utilities for comparing genomic features. Bioinformatics *26*, 841–842.

Ramírez, F., Ryan, D.P., Grüning, B., Bhardwaj, V., Kilpert, F., Richter, A.S., Heyne, S., Dündar, F., and Manke, T. (2016). deepTools2: a next generation web server for deep-sequencing data analysis. Nucleic Acids Res. *44*, W160–W165.

Rao, S., Tortola, L., Perlot, T., Wirnsberger, G., Novatchkova, M., Nitsch, R., Sykacek, P., Frank, L., Schramek, D., Komnenovic, V., et al. (2014). A dual role for autophagy in a murine model of lung cancer. Nat. Commun. *5*, 3056.

Salah, F.S., Ebbinghaus, M., Muley, V.Y., Zhou, Z., Al-Saadi, K.R.D., Pacyna-Gengelbach, M., O'Sullivan, G.A., Betz, H., König, R., Wang, Z.-Q., et al. (2016). Tumor suppression in mice lacking GABARAP, an Atg8/LC3 family member implicated in autophagy, is associated with alterations in cytokine secretion and cell death. Cell Death Dis. *7*, e2205.

Schlie, K., Westerback, A., DeVorkin, L., Hughson, L.R., Brandon, J.M., MacPherson, S., Gadawski, I., Townsend, K.N., Poon, V.I., Elrick, M.A., et al. (2015). Survival of effector CD8+ T cells during influenza infection is dependent on autophagy. J. Immunol. *194*, 4277–4286.

Shankaran, V., Ikeda, H., Bruce, A.T., White, J.M., Swanson, P.E., Old, L.J., and Schreiber, R.D. (2001). IFNgamma and lymphocytes prevent primary tumour development and shape tumour immunogenicity. Nature *410*, 1107–1111.

Starobinets, H., Ye, J., Broz, M., Barry, K., Goldsmith, J., Marsh, T., Rostker, F., Krummel, M., and Debnath, J. (2016). Antitumor adaptive immunity remains intact following inhibition of autophagy and antimalarial treatment. J. Clin. Invest. *126*, 4417–4429.

Stephenson, L.M., Miller, B.C., Ng, A., Eisenberg, J., Zhao, Z., Cadwell, K., Graham, D.B., Mizushima, N.N., Xavier, R., Virgin, H.W., and Swat, W. (2009). Identification of Atg5-dependent transcriptional changes and increases in mitochondrial mass in Atg5-deficient T lymphocytes. Autophagy *5*, 625–635.

Sukumar, M., Liu, J., Ji, Y., Subramanian, M., Crompton, J.G., Yu, Z., Roychoudhuri, R., Palmer, D.C., Muranski, P., Karoly, E.D., et al. (2013). Inhibiting glycolytic metabolism enhances CD8$^+$ T cell memory and antitumor function. J. Clin. Invest. *123*, 4479–4488.

Tarasov, A., Vilella, A.J., Cuppen, E., Nijman, I.J., and Prins, P. (2015). Sambamba: fast processing of NGS alignment formats. Bioinformatics *31*, 2032–2034.

Townsend, K.N., Hughson, L.R.K., Schlie, K., Poon, V.I., Westerback, A., and Lum, J.J. (2012). Autophagy inhibition in cancer therapy: metabolic considerations for antitumor immunity. Immunol. Rev. *249*, 176–194.

Wang, R., Dillon, C.P., Shi, L.Z., Milasta, S., Carter, R., Finkelstein, D., McCormick, L.L., Fitzgerald, P., Chi, H., Munger, J., et al. (2011). The transcription factor Myc controls metabolic reprogramming upon T lymphocyte activation. Immunity *35*, 871–882.

Wei, H., Wei, S., Gan, B., Peng, X., Zou, W., and Guan, J.-L. (2011). Suppression of autophagy by FIP200 deletion inhibits mammary tumorigenesis. Genes Dev. *25*, 1510–1527.

Wei, J., Long, L., Yang, K., Guy, C., Shrestha, S., Chen, Z., Wu, C., Vogel, P., Neale, G., Green, D.R., and Chi, H. (2016). Autophagy enforces functional integrity of regulatory T cells by coupling environmental cues and metabolic homeostasis. Nat. Immunol. *17*, 277–285.

Wherry, E.J., and Ahmed, R. (2004). Memory CD8 T-cell differentiation during viral infection. J. Virol. *78*, 5535–5545.

Wong, C.C., Qian, Y., and Yu, J. (2017). Interplay between epigenetics and metabolism in oncogenesis: mechanisms and therapeutic approaches. Oncogene *36*, 3359–3374.

Xu, X., Araki, K., Li, S., Han, J.-H., Ye, L., Tan, W.G., Konieczny, B.T., Bruinsma, M.W., Martinez, J., Pearce, E.L., et al. (2014). Autophagy is essential for effector CD8(+) T cell survival and memory formation. Nat. Immunol. *15*, 1152–1161.

Yousefi, S., Perozzo, R., Schmid, I., Ziemiecki, A., Schaffner, T., Scapozza, L., Brunner, T., and Simon, H.-U. (2006). Calpain-mediated cleavage of Atg5 switches autophagy to apoptosis. Nat. Cell Biol. *8*, 1124–1132.

Zhang, J.A., Mortazavi, A., Williams, B.A., Wold, B.J., and Rothenberg, E.V. (2012). Dynamic transformations of genome-wide epigenetic marking and transcriptional control establish T cell identity. Cell *149*, 467–482.

STAR★METHODS

KEY RESOURCES TABLE

REAGENT or RESOURCE	SOURCE	IDENTIFIER
Antibodies		
Anti-LC3B	Novus Biologicals	Cat#NB100-2220; RRID:AB_10003146
Anti-p62	Sigma	Cat#P0067; RRID:AB_1841064
Anti-p62	Progen	Cat#CP62-C
Anti-GAPDH	Novus Biologicals	Cat#NB300-221; RRID:AB_10077627
Anti-ATG16L1	MBL	Cat#PM040; RRID:AB_1278757
Anti-Actin	Cell Signaling	Cat#3700; RRID:AB_2242334
Anti-ATG5	Sigma	Cat#A0731; RRID:AB_796188
Anti-Actin	Sigma	Cat# A2066; RRID:AB_476693
Anti-Cleaved Caspase 3	Cell Signaling	Cat# 9664; RRID:AB_2070042
Anti-Ki-67	AbCam	Cat# ab16667; RRID:AB_302459
Anti-CD8	BioXCell	Cat# BE0061; RRID:AB_1125541
Anti-CD4	BioXCell	Cat# BE0086; RRID:AB_1107791
Anti-IgG	Mabtech	Cat# 3321-3-1000; RRID:AB_2123057
Anti-IFNɣ	Mabtech	Cat# 3321-6-250; RRID:AB_2280104
Anti-CD4	Thermo Fisher Scientific	Cat#25-0041-81; RRID:AB_469575
Anti-CD8	Thermo Fisher Scientific	Cat#48-0081-80; RRID:AB_1272235
Anti-CD44	Thermo Fisher Scientific	Cat#12-0441-81; RRID:AB_465663
Anti-CD62L	Thermo Fisher Scientific	Cat#17-0621-81; RRID:AB_469409
Anti-PD-1	Thermo Fisher Scientific	Cat# 11-9981-82; RRID:AB_465467
Anti-CD127	Thermo Fisher Scientific	Cat#12-1271-82; RRID:AB_465844
Anti-CD25	Thermo Fisher Scientific	Cat#17-0251-81; RRID:AB_469365
Anti-FOXP3	Thermo Fisher Scientific	Cat#12-5773-80; RRID:AB_465935
Anti-IFNɣ	Thermo Fisher Scientific	Cat#17-7311-81; RRID:AB_469503
Anti-TNFα	Thermo Fisher Scientific	Cat#12-7321-41; RRID:AB_10854722
Anti-T-Bet	Thermo Fisher Scientific	Cat#12-5825-82; RRID:AB_925761
Anti-Eomes	Thermo Fisher Scientific	Cat#11-4877-41; RRID:AB_2572498
Anti-Tri-methyl histone H3 (Lys27)	Cell Signaling Technology	Cat# 12158
Anti-Tri-methyl histone H3 (Lys27 – ChIP)	Kimura et al., 2008	PMID: 18227620
Anti-Tri-methyl histone H3 (Lys4)	Cell Signaling Technology	Cat# 9751
Chemicals, Peptides, and Recombinant Proteins		
Tamoxifen	Sigma	Cat# T5648
Concanavalin A	Sigma	Cat# 5275
PMA	Sigma	Cat# P1585-1MG
Ionomycin	Sigma	Cat# I9657-1MG
2-NBDG	Thermo Fisher Scientific	Cat# N13195
BPTES	Sigma	Cat# SML0601-5MG
IP buffer	Lorzadeh et al., 2017	PMID: 29286469
Protease inhibitor cocktail	Calbiochem	Cat# 539134
Low salt wash buffer	Lorzadeh et al., 2017	PMID: 29286469
High salt wash buffer	Lorzadeh et al., 2017	PMID: 29286469
ChIP elution buffer	Lorzadeh et al., 2017	PMID: 29286469
MNase dilution buffer	Lorzadeh et al., 2017	PMID: 29286469
MNase master mix	Lorzadeh et al., 2017	PMID: 29286469

(*Continued on next page*)

Continued

REAGENT or RESOURCE	SOURCE	IDENTIFIER
DNA purification master mix	Lorzadeh et al., 2017	PMID: 29286469
End repair master mix	Lorzadeh et al., 2017	PMID: 29286469
A-tailing master mix	Lorzadeh et al., 2017	PMID: 29286469
Adaptor ligation master mix	Lorzadeh et al., 2017	PMID: 29286469
PCR master mix	Lorzadeh et al., 2017	PMID: 29286469
Critical Commercial Assays		
Mouse IFNɣ ELISA	Thermo Fisher Scientific	Cat# 88-7314-22
Seahorse XF Cell Mito Stress Test	Agilent	Cat# 103015-100
Foxp3/Transcription factor staining buffer set	Thermo Fisher Scientific	Cat# 00-5523-00
RNeasy Mini Kit	QIAGEN	Cat# 74104
Fixation/Permeabilization Solution Kit with BD GolgiStop	BD Biosciences	Cat# 554715
Power SYBR Green PCR master mix	Thermo Fisher Scientific	Cat# 4367659
MessageBOOSTER cDNA Synthesis from Cell Lysates Kit	Lucigen	Cat# 75927-958
Zymo RNA Clean and Concentrator-5	Cedarlane	Cat# R1015
Deposited Data		
ChIP-Seq	This paper	GEO: GSE117757
Experimental Models: Cell Lines		
Mouse: e0771	Dr. John Stagg	N/A
Mouse: Tramp-C2	ATCC	Cat# CRL-2731
Mouse: EL4-OVA	ATCC	Cat# CRL-2113
Mouse: MC38	ATCC	Cat#2638
Experimental Models: Organisms/Strains		
Mouse: C57BL/6J	The Jackson Laboratory	Cat# 000664
Mouse: *Atg5*$^{+/-}$ and *Atg5*$^{-/-}$	Dr. Noboru Mizushima	PMID: 16625204
Mouse: *Atg14*$^{+/-}$ and *Atg14*$^{-/-}$	Dr. Tatsuya Siatoh	N/A
Mouse: C57BL/6-Tg(CD8a-cre)1Itan/J	The Jackson Laboratory	Cat# 008766
Mouse; *Atg16L1*$^{+\acute{e}+}$ and *Atg16L1*$^{-\acute{e}-}$	Dr. Aditya Murthy	PMID: 29358708
Mouse: Cre-ER^{T2}	Taconic	Cat# 10471
Mouse: B6.PL-*Thy1*^{a}/CyJ	The Jackson Laboratory	Cat# 000406
Mouse: C57BL/6-Tg(TcraTcrb)1100Mjb/J	The Jackson Laboratory	Cat# 003831
Oligonucleotides		
See Table S1. qPCR primers	This paper	N/A
See Table S2. PCR reverse indexing primers and ChIP-Seq primers	This paper	N/A
Software and Algorithms		
ImageJ	National Institutes of Health	N/A
GraphPad Prism	GraphPad Software Inc	N/A
InForm	Perkin Elmer	N/A
FlowJo	BD Biosciences	N/A
MetaboAnalyst	MetaboAnalyst	N/A
Burrows-Wheeler Aligner	Li and Durbin, 2010	PMID: 20080505
SAMtools	Li et al., 2009	PMID: 19505943
deepTools	Ramírez et al., 2016	PMID: 27079975

CONTACT FOR REAGENT AND RESOURCE SHARING

Further information and requests for resources and reagents should be directed to the Lead Contact, Julian J. Lum (jjlum@bccancer.bc.ca).

EXPERIMENTAL MODEL AND SUBJECT DETAILS

Mice

All animal studies mice were approved by the University of Victoria's Animal Care Committee and were in accordance with the Canadian Council for Animal Care guidelines or Genentech Institutional Animal Care and Use Committee. Atg5 floxed mice (*Atg5*$^{fl/fl}$) (Hara et al., 2006) were crossed to Cre-ER^{T2} (C57BL/6-Gt*(ROSA)26Sor*$^{tm9(Cre/ESR1)Arte}$) and Thy1.1 (B6.PL-Thy1^{a}/CyJ) mice as previously described (Schlie et al., 2015) and were referred to as *Atg5*$^{+/-}$ and *Atg5*$^{-/-}$ mice. A similar strategy was used to generate the *Atg16L1*$^{+/+}$ and *Atg16L1*$^{-/-}$ mice. To induce Cre-mediated deletion of *Atg5*, mice were injected i.p. with 1.5 mg tamoxifen (Sigma-Aldrich) on 4 consecutive days or 1 mg for 3 consecutive days for Atg16L1 prior to tumor implantation. *Atg14*$^{fl/fl}$ mice were backcrossed onto the C57BL/6 background for at least 10 generations. Congenic mice were bred to Cre-ER^{T2} mice and the resulting transgenic mice, referred to as *Atg14*$^{+/-}$ and *Atg14*$^{-/-}$ were used to generate BMC's. For generation of bone marrow chimeras, 6-week old C57BL/6 (wild-type), *Atg5*$^{+/-}$, *Atg5*$^{-/-}$, *Atg14*$^{+/-}$ or *Atg14*$^{-/-}$ mice received 5 days of pre-irradiation water containing antibiotics (Enrofloxacin), which animals remained on until 30 days post radiation. During the first 30 days, animals were placed in an isolator bubble. All equipment for the BMC studies was autoclaved or pre-soaked in Clidox for 10 minutes prior to contact with mice. The irradiation platform was disinfected with Virkon. Recipient mice were given 9.5 Gy radiation on a Varian Truebeam linear accelerator or the Small Animal Radiation Research Platform (SARRP; Xstrahl). 5x10^{6} bone marrow cells were harvested from femurs and tibias of tamoxifen naive *Atg5*$^{+/-}$, *Atg5*$^{-/-}$, *Atg14*$^{+/-}$, *Atg14*$^{-/-}$ or C57BL/6 mice and were injected into the tail vein of irradiated hosts. Chimerism was confirmed 6-8 weeks post-irradiation by saphenous vein bleed and flow cytometry. All BMC studies were performed in SPF facility with irradiated food (*ad lib*) and autoclaved bedding and nesting material for enrichment. Water was provided *ad lib* using an automated system.

Cell culture

e0771 cells, a gift from Dr. John Stagg, were cultured with RPMI-1640 supplemented with 10% FBS, 2.05 mM L-glutamine, 100 U/mL penicillin and 100 μg/mL streptomycin (all from Fisher Scientific). Tramp-C2 cells (ATCC) were cultured in DMEM supplemented with 5% Nu-serum IV (Fisher Scientific), 5% FBS, 2.05 mM L-glutamine, 100 U/mL penicillin, 100 μg/mL streptomycin, 0.005 mg/ml bovine insulin (Sigma-Aldrich) and 10 nM dehydroisoandrosterone (Sigma-Aldrich). MC38 cells were cultured in RPMI-1640 supplemented with 10% FBS, 2mM L-glutamine, 100 U/mL penicillin and 100 μg/mL streptomycin (GIBCO).

METHOD DETAILS

Tumor challenge

8-12 week old female tamoxifen-treated *Atg5*$^{+/-}$ and *Atg5*$^{-/-}$ mice were injected subcutaneously with 1 × 10^{6} e0771 cells in the left mammary fat pad. For Atg16L1 studies, 0.1x10^{6} e0771 cells were injected with a HBSS and matrigel suspension in the mammary fat pad. Male *Atg5*$^{+/-}$ and *Atg5*$^{-/-}$ mice received 5 × 10^{6} Tramp-C2 cells subcutaneously in the right flank. For the MC38 tumor studies, 0.1x10^{6} cells were injected subcutaneously with a HBSS and matrigel suspension. For adoptive cell transfer experiments, 1x10^{6} E.G7-OVA cells were implanted subcutaneously into the flanks of C57BL/6 mice, and on day 11 after implantation, mice received 1 × 10^{6} *Atg5*$^{+/-}$ or *Atg5*$^{-/-}$ CD8+ OTI T cells. Tumors were measured at least three times a week with digital calipers and tumor area was calculated using the formula $mm^2 = (length \times width)$. For Atg16L1 studies, tumors were measured at least twice a week with digital calipers and tumor volume calculated using the formula $mm^3 = (\text{longer measurement x shorter measurement}^2) \times 0.5$. In experiments where CD8+ T cells were depleted, *Atg5*$^{+/-}$ and *Atg5*$^{-/-}$ mice were treated with 200 μg of control IgG (BioXcell) or anti-CD8 (clone 2.43, BioXcell) depleting antibody at day −1, +1, +7 and +15 relative to tumor cell implantation. CD8 T cell depletion was confirmed by flow cytometry.

Immunohistochemistry

e0771 tumors from *Atg5*$^{+/-}$ and *Atg5*$^{-/-}$ mice were excised and fixed in 10% formalin. 4 μM sections were depraffinized and subjected to antigen retrieval using a decloacking chamber and Rodent M decloacker (Biocare Medical). Rabbit anti-cleaved caspase 3 (Cell Signaling) or rabbit anti-Ki-67 (AbCam) was incubated at room temperature for 30 minutes. Following washing, MACH2 anti-rabbit-HRP polymer was applied for 30 minutes at room temperature followed by DAB reagent (Biocare medical). Slides were counterstained with hematoxylin (Biocare Medical), dried and coverslipped using Ecomount (Biocare medical). Scoring of tumor tissue was performed by taking 3-5 images at 20X magnification using the Nuance Multispectral Imaging Software on an Olympus BX53 microscope. Cleaved caspase-3 was scored using signal thresholding, and Ki-67-positive cells were enumerated using InForm Software Analysis.

Western blotting

For immunoblotting of Atg5, Atg14, LC3B, Atg16L1 and p62, splenocytes were lysed in RIPA buffer (50 mM Tris-HCl pH 7.4, 1% NP-40, 0.25% Na-deoxycholate, 150 mM NaCl, 1 mM EDTA) containing complete protease inhibitor cocktail, and phosphatase inhibitor cocktail for 30 min at 4°C. After centrifugation at 13,000 g for 15 min at 4°C, supernatant was obtained and stored at −80°C. Lysates were quantified using BCA assay (Thermo Fisher) and equal amounts loaded onto 4%–12% gradient SDS-PAGE gels.

Protein was transferred onto nitrocellulose or PVDF membranes and immunoblots for Atg5, Atg14, LC3B, Atg16L1, p62, GAPDH and actin performed using respective antibodies (listed in Key Resources).

IFNγ ELISPOT and ELISA

ELISPOT plates (Millipore) were coated with 10 μg/mL anti-mouse IFNγ antibody overnight at 4°C. Plates were then washed and blocked with complete RPMI for 2 hours at 37°C, 5% CO_2. Splenocytes were harvested from tumor bearing mice and processed into single cell suspensions by pressing through a 40 μM screen in complete RPMI. Red blood cells were lysed with ACK lysis buffer. $1x10^6$ splenocytes were plated per well and stimulated with $1x10^5$ e0771 or Tramp-C2 cells, 5 μg/mL SPAS-1 peptide or 5 μg/mL Concanavalin A (Sigma) as a positive control for 20 hours at 37°C and 5% CO_2. Plates were then washed and incubated with 1 μg/mL biotinylated anti-IFNγ secondary antibody (Mabtech) for 2 hours at 37°C. Plates were developed with Vectastain ABC Elite and Vectastain AEC substrate (Vector Lab's) according to the manufacturer's instructions. For IFNγ ELISA, serum was collected from tumor bearing mice and frozen in aliquots at −80°C. IFNγ ELISA was performed according to the manufacturer's instructions.

T cell stimulation

For intracellular cytokine staining, splenocytes isolated from *Atg5*$^{+/-}$ and *Atg5*$^{-/-}$ mice were stimulated for 6 hours with 25 ng/mL PMA and 1 μg/mL ionomycin in the presence of 10 μg/mL Brefeldin A (Sigma) and Golgi stop (BD Biosciences). Alternatively, cells were stimulated with plate-bound CD3 (5 μg/mL; BD Biosciences) and CD28 (1 μg/mL; BD Biosciences) for 72 hours. For histone trimethylation analysis, splenocytes were isolated from *Atg5*$^{+/-}$ or *Atg5*$^{-/-}$ CreER^{T2} Thy1.1 OTI mice and stimulated for 2 hours with 2 μg/mL SIINFEKL peptide. Cells were washed and placed into media containing 100 U/mL of IL-2 and treated with 3 μM of tamoxifen to induce Atg5 deletion. Following *in vitro* stimulation, cells were stained with intracellular cytokines using the fixation and permeabilization kit (BD Bioscience) according to the manufacturer's instructions. For metabolic treatments, cells were cultured overnight in the presence or absence of glucose or 10 μM BPTES followed by PMA plus ionomycin stimulation as above.

Flow cytometry

For analysis of cell surface or nuclear markers, cells were stained with CD4, CD8, CD44, CD62L, CD127, PD-1, CD25, FOXP3 (all eBioscience), or H3K27me3 (Cell Signaling) in complete medium for 20 minutes at 4°C. For intracellular cytokine staining, isolated splenocytes were stimulated with PMA/ionomycin for 6 hours in the presence of GolgiStop plus Brefeldin A according to the manufacturer's instructions (BD Bioscience). For analysis of mitochondrial mass, cells were stained with 40 nM MitoTracker Green (Life Technologies) for 20 minutes or MitoSox Red (Life Technologies) for 10 minutes, respectively, at 37°C. Glucose uptake was monitored by incubating cells with 100 μM 2-NBDG (Life Technologies) for 30 minutes at 37°C.

Quantitative RT-PCR

RNA from tumors, tumor draining lymph nodes, or splenic CD8+ T cells was isolated with an RNeasy Mini kit (QIAGEN), followed by cDNA synthesis with qScript cDNA synthesis kit (Quanta Biosciences) or MessageBOOSTER cell lysates to cDNA synthesis kit (Lucigen). RNA was concentrated using an RNA Clean & Concentrator kit (Zymo). Gene expression was assessed by real-time PCR with PerfeCTa SYBR Green SuperMix for iQ (Quanta Biosciences) on a MyiQ real-time PCR detection system (BioRad). Primer sequences for each target gene can be found in Table S2. Results were calculated using the ΔCt method relative to *actin* and were displayed as $2^{-\Delta Ct}$.

Metabolism assays

CD8+ T cells were isolated from tumor bearing mice using an EasySep CD8+ T cell isolation kit (StemCell) according to the manufacturer's instructions. 350,000 cells were plated in non-buffered RPMI supplemented with 25 mM glucose, 2 mM pyruvate and 2 mM glutamine. Measurements were obtained under basal conditions and in response to 1 μM Oligomycin, 2 μM FCCP and 0.5 μM Antimycin A/Rotenone. OCR and ECAR were measured on a XFe96 Extracellular Flux Analyzer (Seahorse).

Metabolomics

For global metabolomic analysis, CD8+ T cells were isolated from tumor bearing mice using EasySep CD8+ T cell isolation kit (StemCell). Cells were washed with 0.9% saline solution, resuspended in 80% methanol and snap frozen in liquid nitrogen. Samples were subjected to repeated freeze-thaws, dried using a SpeedVac, and frozen at −80°C. The samples were analyzed by LC-MS as previously described (Mullen et al., 2014). The dataset of significantly altered metabolites was imported into MetaboAnalyst 3.0 for pathway enrichment analysis and heatmap generation.

Low input native ChIP-Seq

Low input native ChIP-seq was performed as previously described (Lorzadeh et al., 2016). In brief, cells were lysed in 0.1% Triton X-100 and Deoxycholate supplemented with protease inhibitor cocktail. Chromatin were digested by Microccocal nuclease (MNase) at room temperature for 5 minutes and 0.25mM EDTA was used to stop the reaction. Antibodies against epitopes of interest (H3K4me3 and H3K27me3) and digested chromatin were incubated with anti-IgA magnetic beads for 2 and 1.5 hours respectively. Pre-cleared chromatin was incubated with antibody-bead complex over night in IP buffer (20 mM Tris-HCl pH 7.5, 2 mM EDTA, 150 mM NaCl, 0.1% Triton X-100, 0.1% Deoxycholate) at 4°C. IPs were washed 2 times by Low Salt (20 mM Tris-HCl pH 8.0, 2 mM EDTA, 150 mM NaCl, 1% Triton X-100, 0.1% SDS) and High Salt (20 mM Tris-HCl pH 8.0, 2 mM EDTA, 500 mM NaCl, 1% Triton X-100, 0.1% SDS) wash buffers. IPs were eluted in elution buffer (1% SDS, 100 mM Sodium Bicarbonate) for 1.5 hours at 65°C. Histones were digested by Protease for 30 min at 50°C and DNA fragments were purified using Sera Mag magnetic beads in 30% PEG. Illumina sequencing libraries were generated by end repair, 3′ A-addition, and Illumina sequencing adaptor ligation. Libraries were then indexed and PCR amplified and sequenced on Illumina HiSeq 2500 sequencing platform following the manufacturer's protocols (Illumina, Hayward CA.). The ChIP-Seq data have been deposited in GEO, under accession number GEO: GSE117757.

QUANTIFICATION AND STATISTICAL ANALYSIS

Evaluation of tumor growth curves was performed using a two-way ANOVA. A Student t test was used when comparing the means of two groups, and a one-way ANOVA was used when comparing more than two groups. Values less than 0.05 were considered statistically significant (*$p < 0.05$; **$p < 0.01$; ***$p < 0.001$; ****$p < 0.0001$). ChIP-seq sequence reads were aligned to GRCm38 using Burrows-Wheeler Aligner (BWA) 0.7.6a (Li and Durbin, 2010) and converted to bam format by Sambamba (version 0.5.5) (Tarasov et al., 2015). Sequence reads with BWA mapping quality scores < 5 were discarded and reads that aligned to the same genomic coordinate were counted only once in the profile generation. H3K4me3 enriched regions were identified by MACS2 (Feng et al., 2012)) in pair-end mode at q-value of 0.01. Enriched promoters were identified by overlapping of MACS2 identified peaks with +/2kb of TSS of protein coding genes (Ensemble mm10v84) using bedtools (Quinlan and Hall, 2010) with –f 0.5 parameter. Normalized tag density was generated using HOMER v4.10 (Heinz et al., 2010). ChIP-seq signal was normalized to the depth of libraries (excluding duplicated reads and reads falling within the ENCODE mm10 blacklist regions) and the length of the promoters. Input control normalized ChIPseq tracks were generated using MACS2.

DATA AND SOFTWARE AVAILABILITY

The accession number for the ChIP-Seq data reported in this paper is GEO: GSE117757.